Bifacial All-Perovskite Tandem Solar Cells

Bo Chen,^{1†} Zhenhua Yu,^{1†} Arthur Onno,² Zhengshan Yu,² Shangshang Chen,¹ Jiantao Wang,¹ Zachary C. Holman,² Jinsong Huang¹*

¹ Department of Applied Physical Sciences, The University of North Carolina at Chapel Hill, Chapel Hill, NC 27599, USA

² School of Electrical, Computer, and Energy Engineering, Arizona State University, Tempe,
AZ 85287, USA

* Correspondence: jhuang@unc.edu (JH)

Abstract: The efficiency of all-perovskite tandem devices falls far behind the theoretical efficiency limit, mainly because widening bandgap fails to increase open-circuit voltage. Here we report all-perovskite tandem structures with an equivalent efficiency of 29.3% under back-to-front irradiance ratio of 30%, which not only increase energy yield but also reduce the required bandgap of wide-bandgap cell to minimize open-circuit voltage deficit, even though its performance under only front irradiance is not ideal. Bifacial device needs a sputtered rear transparent electrode, which could reduce photon pathlength and deteriorate stability of Pb-Sn perovskites. We embed a light scattering micrometer-sized particle layer into perovskite to trap light, which effectively increases absorptance by 5-15% in infrared region. Using a non-acidic hole-transport-layer dramatically stabilizes hole-extraction interface by avoiding proton-accelerated formation of iodine. These two strategies together increase efficiency of semitransparent Pb-Sn cells from 15.6% to 19.4%, which enables the fabrication of efficient bifacial all-perovskite tandem devices.

INTRODUCTION

Monolithic all-perovskite tandem solar cells have a higher theoretical efficiency limit than single junction perovskite solar cells and silicon solar cells (1,2). Compared to other tandem photovoltaic (PV) technologies, all-perovskite tandems have the distinctive advantage that the fabrication of both light absorbing layers is compatible with low-cost, low-temperature solution processing techniques (3,4). Tremendous progress has been made on all-perovskite tandem solar cells over the past six years, and the efficiency has increased to 28.0% (5-18). However, the full potential of all-perovskite tandem solar cells has not been demonstrated, because it should have a realistic efficiency upper limit of approximately 30% (1,2). In a series-connected (2-terminal) monolithic all-perovskite tandem solar cell, the ideal marriage is between a ~1.20 eV narrow bandgap (NBG) bottom cell and a 1.75–1.85 eV wide bandgap (WBG) top cell (1). For the NBG bottom cell, Tong et al. reported a quasi-two-dimensional additive engineering method that significantly increased the carrier lifetime to ~9.2 µs and achieved a high efficiency (17). The efficiency of reported all-perovskite tandem solar cells is primarily limited by the large opencircuit voltage deficit—defined as Woc=Eg/e-Voc, where Eg is the bandgap of the perovskite absorber, e is the elementary charge, and V_{OC} is the open-circuit voltage—of the WBG perovskite top cell (5-16). Widening the bandgap of the metal-halide perovskite absorber beyond 1.68 eV often failed to further increase the device V_{OC} (19-25), where W_{OC} enlarged with the increase of bandgap. Despite extensive efforts by the global community to overcome this challenge (26-31), in the best reported all-perovskite tandem devices, the 1.75–1.85 eV WBG cells have V_{OC} values in the range of 1.20–1.23 V, with a corresponding W_{OC} of 0.54–0.59 V (10-16). In comparison, W_{OC} as low as 0.31–0.35 V have been achieved for 1.50–1.60 eV perovskite solar cells (32-34). The larger W_{OC} in WBG perovskites has been ascribed to ion-migration-induced phase segregation

(35) and to the large density of defects in mixed halide perovskites (even in films free of phase segregation) (36,37), which might both be intrinsic to WBG perovskites with mixed halides.

Bifacial PV can harvest more of the available solar resource, by not only absorbing direct and diffuse light from their front surface but also diffuse light and light reflected of the ground the albedo light—from their rear surface (38). This increases the energy yield compared to conventional mono-facial PV technologies (39-43), and bifacial PV is now considered as one of the most promising pathways to increase the energy yield of silicon-based PV modules. A notable advantage of using bifacial structures for monolithic all-perovskite tandem solar cells is that the optimal bandgap for the WBG cell can be reduced to achieve a smaller Woc, because the additional photocurrent generated in the NBG bottom cell from rear irradiance must be balanced by the WBG top cell through reducing WBG perovskite bandgap (40-43). Even though the technological barrier is not necessarily larger than the one to transition from mono-facial silicon PV modules to bifacial PV modules, the bifacial all-perovskite tandem solar cells with transparent conductive oxide (TCO) electrode on both sides have not been studied yet. To date, TCO sputtering is the most common approach to deposit transparent electrodes on perovskite absorbers. This method requires the deposition of a SnO₂ buffer-layer by atomic-layer-deposition (ALD-SnO₂) at typical temperature of 70 °C—100 °C to avoid sputtering damage to the perovskite material (14,44,45). However, when transforming the rear electrode from metal to TCO, it is a challenge to achieve high photovoltaic performance of NBG cell which are made of mixed Pb-Sn perovskites (46,47). Prasanna et al. found that the charge extraction became worse after thermal annealing at 85 °C for the NBG Pb-Sn perovskite solar cells with the commonly used hole transporter of poly(3,4ethylenedioxythiophene) polystyrene sulfonate (PEDOT:PSS) (46). Xiao et al. utilized low ALD temperature of 70 °C to avoid the efficiency drop of NBG cells on PEDOT:PSS after deposition

of ALD-SnO₂, however, the device efficiency still dropped to less than 80% of initial value after thermal annealing at 85 °C for only 80 hours (*14*). Moreover, the pathlength of photons within the perovskite absorber is reduced from a double pass in mono-facial device (thanks to reflection on the rear metal electrode) to a single pass in bifacial device, which decreases the light absorption and limits the short-circuit current density (J_{SC}) of Pb-Sn perovskites. Further increasing the film thickness didn't guarantee an increased J_{SC} in the semitransparent devices, because the film quality became worse for thick Pb-Sn perovskite films (*10*). Recently, several strategies have been reported to increase the carrier diffusion length of Pb-Sn perovskite films (*10*, *16*), but the optimal thickness are still too thin to absorb most infrared light in semitransparent Pb-Sn perovskite solar cells, due to their small absorption coefficient in this wavelength range (*10-16*).

Here we reported methods to improve the performance of semitransparent NBG Pb-Sn perovskite solar cells by embedding the light trapping structures to increase the photon pathlength and by replacing the acidic PEDOT:PSS with neutral PEDOT for better thermal stability. Instead of using thicker Pb-Sn perovskite films—which incidentally contain more toxic lead—we demonstrated an alternative strategy to extend the photon pathlength without having to increase the film thickness. We found that acidic PEDOT:PSS hole transport layer (HTL) drove the formation of I₂, which in-turn quickly oxidized the Pb-Sn perovskite and decreased the charge collection efficiency after deposition of ALD-SnO₂, thus, a non-acidic PEDOT HTL was introduced to overcome this issue. The resulting high-efficiency semitransparent NBG Pb-Sn perovskite cells were used to fabricate efficient bifacial all-perovskite tandem solar cells. Annual yield simulations confirm that bifacial all-perovskite tandem technology not only improves the annual energy yield compared to the mono-facial case, but also relaxes the constraint on the

bandgap of the top cell, allowing the use of a lower-bandgap top cell and, thus, minimizing the Woc.

RESULTS

Non-acidic HTL to improve the thermal stability of Pb-Sn perovskite cells

Bifacial all-perovskite tandem solar cell needs an efficient and stable semitransparent NBG sub-cell. Therefore, it is essential to improve the compatibility of charge transport layers with Pb-Sn perovskites, which can not only improve the device stability in photovoltaic application but also avoid the efficiency drop during high temperature deposition of sputtering buffer layer. We found that the efficiency of 1.21 eV Cs_{0.2}FA_{0.8}Pb_{0.5}Sn_{0.5}I₃ perovskite solar cells fabricated on acidic PEDOT:PSS as HTL was dramatically reduced from 19.9% to 17.2% after deposition of ALD-SnO₂ at 85 °C when compared to the control device with thermal evaporated BCP/Cu layers, with dramatic reductions in J_{SC} and V_{OC} (Fig. 1a). The reduction in J_{SC} can be traced to a decrease of the external quantum efficiency (EQE) across the full spectrum (Fig. 1a, inset)—even though the absorptance of the devices remains unchanged (Fig. S1)—which indicates that the carrier collection efficiency became poor due to formation of defects in samples after deposition of ALD-SnO₂. Post-deposition annealing of ITO/PEDOT:PSS/Pb-Sn samples inside N₂-filled gloveboxes (or ITO/PEDOT:PSS/Pb-Sn perovskite/C₆₀ samples inside ALD vacuum chamber without any Sn or water precursor pulse) followed with thermal evaporation of C₆₀/BCP/Cu (or BCP/Cu) also led to large reductions in J_{SC} and V_{OC} (Fig. S2). This reveals that the reduction in efficiency of samples with an ALD-SnO₂ buffer layer stems from the poor thermal stability of Pb-Sn perovskites on HTL of acidic PEDOT:PSS. We changed the HTL from acidic PEDOT:PSS to neutral PEDOT, where these two HTLs showed similar work function as measured by ultraviolet photoelectron

spectroscopy (UPS) (Fig. 1b). The Pb-Sn perovskite solar cells on neutral PEDOT did not show such large decrease in J_{SC} and V_{OC} when combined with an ALD-SnO₂ buffer layer deposited at 85 °C (Fig. 1c). Moreover, device fabricated on neutral PEDOT maintained 80% of initial efficiency after thermal stress at 85 °C for 1000 hours, which is better than the counterpart fabricated on acidic PEDOT:PSS (Fig. 1d and Fig. S3). Benefit from this improvement in thermal stability when using a non-acidic HTL, the mean efficiency of semitransparent NBG cells significantly increases from 15.6% for devices made on acidic PEDOT:PSS to 18.2% for devices fabricated on neutral PEDOT (Fig. 1e and Fig. S4). The main PCE drop of the semitransparent NBG Pb-Sn cells on neutral PEDOT come from the infrared-absorption loss due to the single-pass photon pathlength (Fig. 1c).

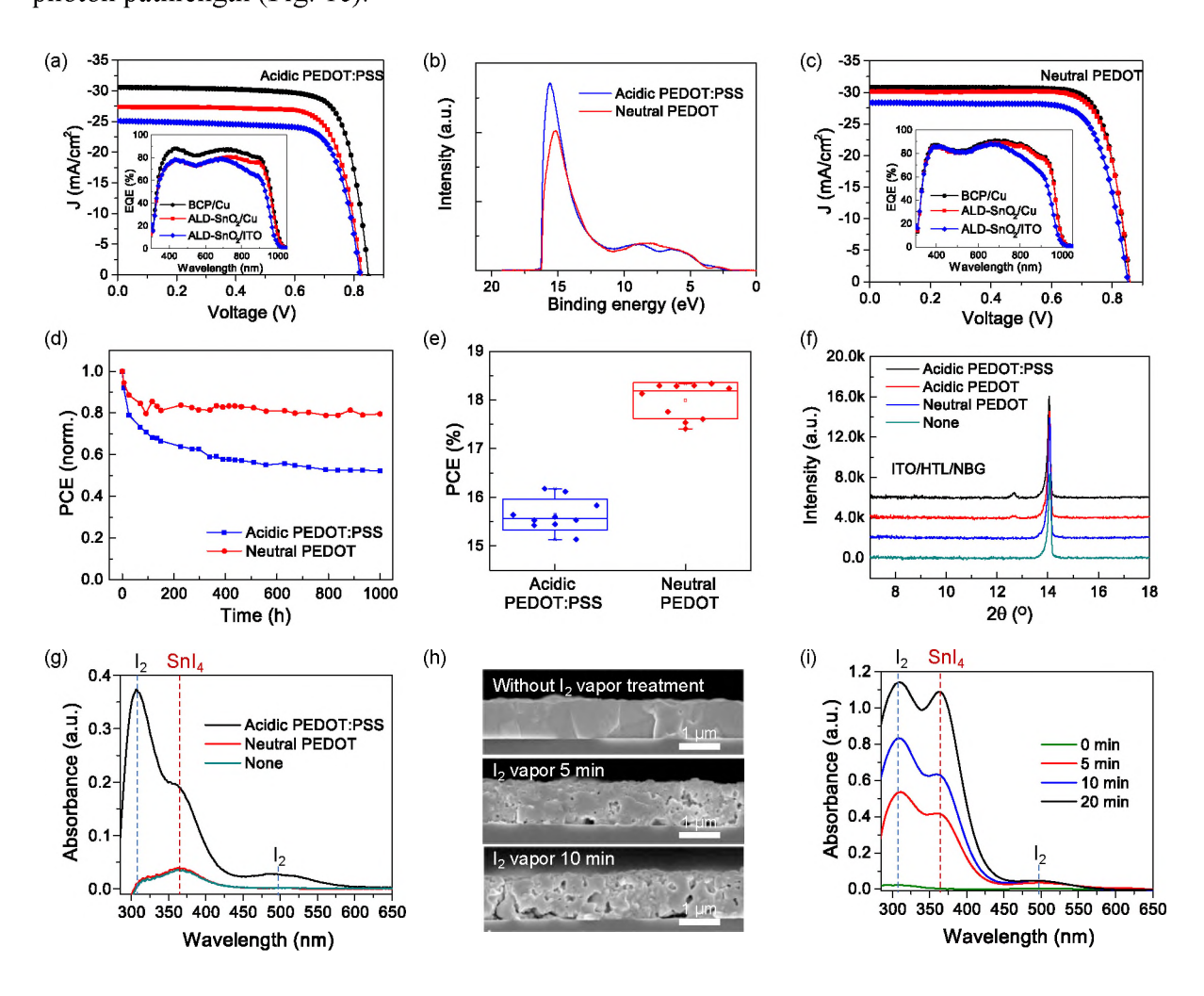


Fig. 1. Improving thermal stability of NBG Pb-Sn perovskite cell with neutral PEDOT. (a) J-V curves and EQE curves of 1.21 eV Cs_{0.2}FA_{0.8}Pb_{0.5}Sn_{0.5}I₃ perovskite solar cells fabricated on acidic PEDOT:PSS with C₆₀/BCP/Cu, C₆₀/ALD-SnO₂/Cu, and C₆₀/ALD-SnO₂/ITO electron transport layers (ETL) and cathodes. (b) Measured work function of acidic PEDOT:PSS and neutral PEDOT by UPS. (c) J-V curves and EQE curves of Pb-Sn cells fabricated on neutral PEDOT with C₆₀/BCP/Cu, C₆₀/ALD-SnO₂/Cu, and C₆₀/ALD-SnO₂/ITO ETL and cathodes. (d) Thermal stability of semi-transparent Pb-Sn cells fabricated on acidic PEDOT:PSS and on neutral PEDOT and kept at 85 °C in gloveboxes for 1000 hours. (e) Efficiency distribution of 10 semitransparent cells fabricated on acidic PEDOT:PSS and neutral PEDOT, respectively. The box indicates the standard deviation and the line inside box represents the mean value. (f) XRD patterns of the Pb-Sn perovskite films deposited on different HTLs and bare ITO/glass substrate after post-deposition annealing at 130 °C for 45 min. (g) Absorptance spectra of toluene solutions in which Pb-Sn perovskite films were soaked at 85 °C for 48 hours, where Pb-Sn perovskite films were fabricated on acidic PEDOT:PSS, neutral PEDOT, and bare ITO/glass substrate, respectively. (h) Crosssectional SEM images and (i) absorptance spectra of reaction productions from Pb-Sn perovskite films before and after I_2 vapor treatment in sealed vials for different time lengths. Following the I_2 vapor treatment, the samples were taken out of the vials and annealed at 50 °C for 3 min in N_2 filled glovebox to sublimate the adsorbed I₂, the reaction products were then extracted by toluene for absorptance measurement.

The mechanism of different thermal stability of Pb-Sn perovskite cells on different HTLs was investigated. We compared the degradation of Pb-Sn perovskite films fabricated on acidic PEDOT:PSS, acidic PEDOT, neutral PEDOT, and bare ITO/glass substrate. After post-deposition

annealing at 130 °C for 45 min, an XRD peak at 12.7°—associated with the formation of PbI₂ (48)—appears for perovskite films deposited on acidic PEDOT:PSS and acidic PEDOT, but does not appear for films deposited on neutral PEDOT or bare ITO/glass (Fig. 1f). Hence, the intrinsic thermal stability of the Pb-Sn perovskite film is good enough to avoid decomposition under such thermal stress. The responsibility of potential variations in grain structure between samples—due to the different substrates used—was excluded, as the same behavior was observed on samples where the HTLs were applied on top of the perovskite films (Fig. S5). It is noted that the HTLfree Cs_{0.2}FA_{0.8}Pb_{0.5}Sn_{0.5}I₃ perovskite solar cell fabricated on bare ITO/glass substrate didn't show obvious degradation after deposition of ALD-SnO₂ at 85 °C (Fig. S6a), while the device on acidic PEDOT showed large loss of efficiency (Fig. S6b), compared with the control devices with thermally evaporated BCP/Cu. Grazing incidence X-ray diffraction patterns in Fig. S7 show that decomposition of the Pb-Sn perovskite film started from acidic PEDOT: PSS/perovskite interface. This indicates the acidic HTL is the source of the reduction in performance. We found that the acidic PEDOT:PSS can oxidize iodide in perovskites to iodine (I₂) which further oxidize Sn²⁺ in Pb-Sn perovskite into Sn⁴⁺. Fig. 1g demonstrates the formation of I₂ as well as SnI₄ in Pb-Sn perovskite film deposited on acidic PEDOT:PSS after annealing the film in toluene solution at 85 °C for 2 days. Comparatively much less I₂ and SnI₄ were observed for the films deposited on neutral PEDOT and bare ITO substrate after same thermal stress. In addition, we observed that the formation of I₂ can cause severe structural damage to the mixed Pb-Sn perovskite, a phenomenon not observed in Pb-only perovskites. To demonstrate this, we sealed mixed Pb-Sn perovskite and Pb-only perovskite films in vials filled with sublimated I₂ vapor at room temperature. As shown in Fig. 1h, many voids formed inside the Pb-Sn perovskite film within 20 min, which was accompanied by the formation of large amounts of I₂ and SnI₄ (Fig. 1i) and a change in the

composition of the material (Fig. S8). Conversely, Pb-only perovskite was more resistant to I₂ vapor compared to mixed Pb-Sn perovskite (Fig. S9). Thus, the mechanism behind the poor thermal stability of Pb-Sn perovskite films is tied to the use of an acidic HTL, and this issue can be overcome using neutral PEDOT.

Light-trapping structure for enhanced light absorption

Even after addressing the HTL-induced perovskite instability, we still observed a J_{SC} loss when transforming from opaque devices to semitransparent devices. This reduction in J_{SC} by 1.8 mA/cm² in Fig. 1c comes from the reduced EQE at long wavelengths (>700 nm) (Fig. 1c, inset), due to the removal of the reflecting back metal electrode and the associated reduction in photon pathlength. Therefore, we need to increase the photon pathlength to improve the J_{SC} of semitransparent NBG perovskite solar cells. As illustrated in Fig. 2a, we embedded light-scattering particles in the Pb-Sn perovskite film to trap light in this layer. In principle, any inert material that is, chemically stable with metal-halide perovskites—with a refractive index lower than that of the perovskite absorber can be a candidate to fabricate such light-scattering particles. Compared to other light scattering particles, we chose cation-exchange-resin particles in here, because besides the light scattering function those resin particles can have an additional function of locking the Pb in perovskite devices even when the PV modules are completely broken as reported in our previous studies (49,50). There is no noticeable reaction between the resin-particle layer and the Pb-Sn perovskite even at elevated temperature (Fig. S10). The resin-particle layer deposited on ITO/glass exhibits excellent transparency, with no noticeable change in absorption (Fig. S11). These cationexchange resins have a porous structure with a nanoparticle size of approximately 40 nm, after finely powdered by high energy ultrasonic processor to form particle suspension, a non-continuous

resin-particle layer with random height distribution and surface coverage of ~50% was formed by spin-coating resin-particle suspension onto the neutral PEDOT HTL (Fig. 2b and Fig. S12). Considering particle size of close to or larger than the wavelength of photons is desired to have excellent scattering effect, but particle size of several micrometers would cause coverage issue of the light scattering particles by perovskite film, we controlled the thickness of resin-particle layer close to 1 micrometer (µm). This is much thicker than the mesoporous resin layer thickness of \sim 300 nm in our previous Pb adsorbing study (49), where a thin layer of \sim 300 nm doesn't have good light-scattering effect for long wavelength photons. The mesoporous light-scattering layer with thickness close to 1 µm does not impair the formation of a continuous Pb-Sn perovskite layer. As shown in the top-view and cross-sectional SEM images, 1200 nm thick Pb-Sn perovskite film fully cover the resin-particle layer (Fig. 2c-d). Compared to the planar semitransparent device with a J_{SC} of 28.4 mA/cm², the semitransparent device with a resin-particle layer exhibited an improved J_{SC} of 30.2 mA/cm² with no reduction in V_{OC} and FF (Fig. 2e and Fig. S13), and an increase in EQE, particularly at long wavelengths (Fig. 2f). This further improved the mean efficiency of semitransparent Pb-Sn perovskite solar cells from 18.2% to 19.4% (Fig. 2g and Fig. S13).

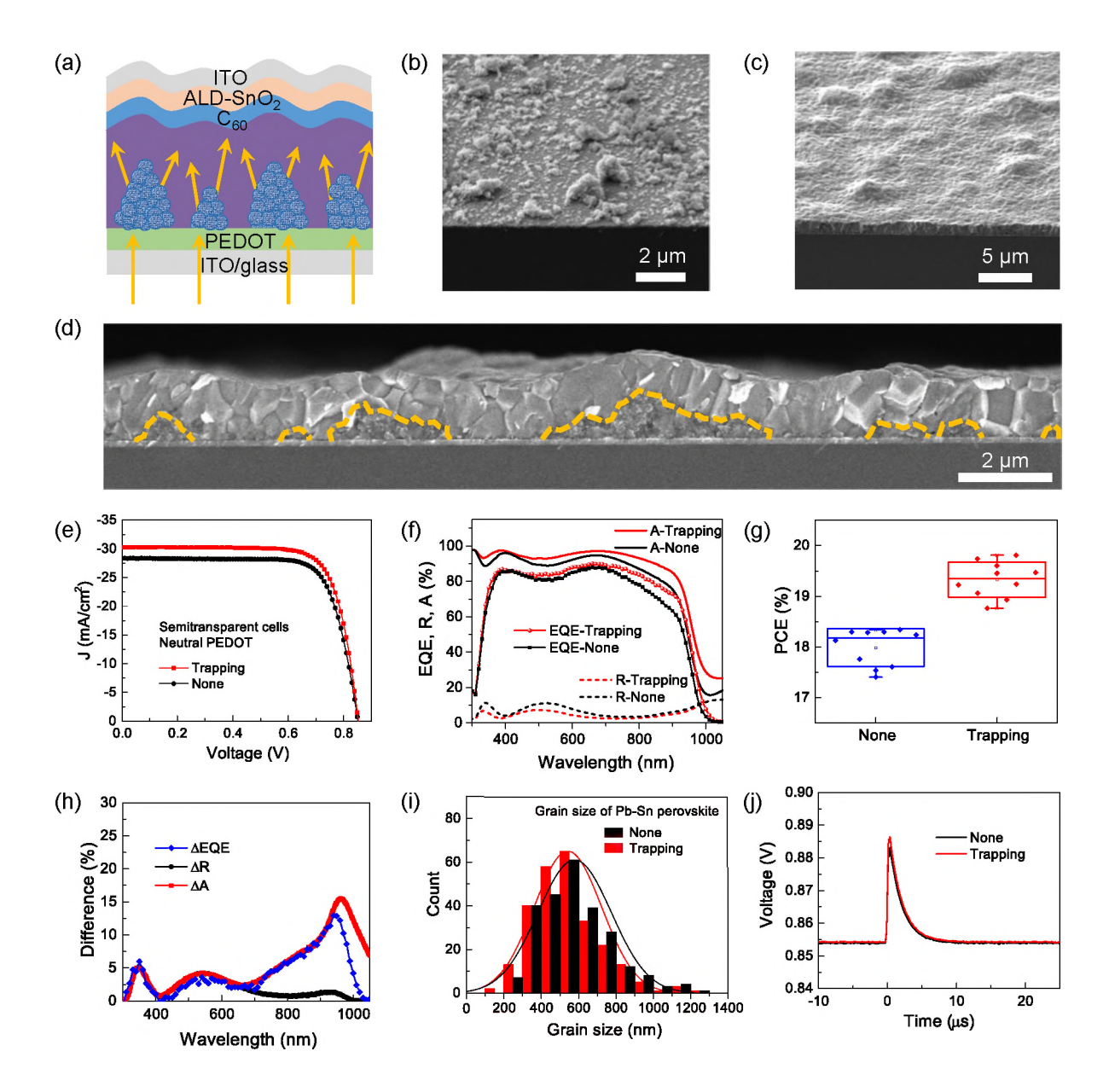


Fig. 2. Light-trapping structure for enhanced light absorption in semitransparent NBG cells. (a) Schematic illustration of the increased photon pathlength through incorporation of light-trapping scattering particles in the NBG perovskite film. 60°-tilted SEM images of (b) resin particles on ITO/glass substrate and (c) Pb-Sn perovskite film on resin-particle layer. (d) Cross-sectional SEM image of Pb-Sn perovskite film on resin-particle layer. (e) J–V curves, (f) EQE, reflectance (R), and absorptance (A), and (g) efficiency distribution of semitransparent Pb-Sn single junction cells on neutral PEDOT with and without light-trapping resin-particle layer under front illumination.

The box in (g) indicates the standard deviation and the line inside box represents the mean value.

(h) Difference in EQE, R, and A between semitransparent Pb-Sn solar cells fabricated with and without a light-trapping layer. (i) Grain size distribution of Pb-Sn perovskite films fabricated on neutral PEDOT without and with light-trapping layer. (j) TPV under AM1.5G illumination with extra laser-pulse excitation for Pb-Sn perovskite cells without and with light-trapping layer.

To understand the mechanism behind the increase in J_{SC} and EQE, we compared the changes in EQE (ΔEQE), reflectance spectrum (ΔR), and absorptance spectrum (ΔA) between semitransparent NBG devices with and without light-trapping resin-particle layer when illuminated from the HTL side (Fig. 2h). In the 700–1100 nm wavelength range—which is the working window for NBG bottom-cells in tandem devices—the integrated J_{SC} under 1-sun front illumination increased by 1.19 mA/cm². Absorptance in the infrared region increases by 5–15% with embedded resin-particles (Fig. 2h). The EQE enhancement matches this increase in absorptance, with correspondingly minimal contribution from the reduction in reflectance. This confirms that the embedded particle layer exhibits the expected light-trapping effect and can increase the photon pathlength in Pb-Sn perovskite solar cells. In the 300-700 nm wavelength range—where most short-wavelength photons are fully absorbed with one pass through the thick Pb-Sn perovskite film and, thus, no scattering effect is needed—the EQE is also improved, resulting in an integrated J_{SC} increase of 0.46 mA/cm² under 1-sun front illumination. The EQE enhancement in this wavelength region matches the reduction in reflectance, indicating that the light-trapping resin-particles also have an anti-reflection function due to change of interference from the device. The haze measurement in Fig. S14 shows that the resin-particle layer has a good light scattering effect across the working window of all-perovskite tandem solar cells. As a result,

it increases the photon pathlength, allows more long wavelength photons to be absorbed by perovskite layer, and also shifts the interference pattern at short wavelength region (Fig. 2f and Fig. S15).

Furthermore, we investigated the influence of resin particles on the morphology and optoelectronic properties of Pb-Sn perovskite films. There was no obvious difference in grain-size distributions (Fig. 2i and Fig. S16) between Pb-Sn perovskite films fabricated with and without light-trapping resin-particle layer. Transient photovoltage (TPV) measurement in Fig. 2j and transient photocurrent (TPC) measurement in Fig. S17 of Pb-Sn perovskite solar cells showed that the carrier recombination lifetime maintained at ~1.85 μs and TPC transit time kept at ~35 ns after embedding the light-trapping resin-particles, where the calculated carrier diffusion length maintained at ~1.5 μm for efficient charge extraction across the Pb-Sn perovskite film. As proved in our previous study (49), the perovskites can infiltrate into mesoporous resin-particle layer, which enables the holes generated at the perovskite layer to be extracted by the ITO/PEDOT interface without being blocked by resin particles.

Performance of bifacial all-perovskite tandem devices

The performance of bifacial all-perovskite tandem devices fabricated with these light-trapping resin-particle structures was characterized. The bifacial tandem devices harvest both direct (and diffuse) incident sunlight from the front WBG side and additional albedo light from the rear NBG side (Fig. 3a). Different from bifacial single junction cells, which typically measure independent efficiencies under only front illumination and only rear illumination that give a bifaciality factor to quantify their ratios (39,43,51), there would be a large current mismatch between sub-cells for the bifacial tandem solar cells when light only illuminating from one side,

thus bifaciality factor doesn't reflect the actual performance of bifacial tandem cells. An appropriate metric to quantify and compare the power production of bifacial tandem devices under applications with albedo light is the "equivalent efficiency", which is the efficiency of a corresponding mono-facial PV device with the same area generating the same power under the same testing conditions (39,43,51). The schematic of the stack of fabricated bifacial all-perovskite tandem solar cells with materials and thickness of each layer was present in Fig. S18. Fig. 3b shows an SEM image of a bifacial all-perovskite tandem solar cell with the embedded light-trapping structure at NBG sub-cell near PEDOT side to scatter the infrared light. Fig. 3c shows that, as expected, the light-trapping structure increased the EQE of the NBG sub-cell in bifacial tandem devices with front illumination (that is light coming from the WBG side), resulting in a 0.9 mA/cm² increase in J_{SC} from the NBG bottom cell under 1-sun illumination. No change in EQE was observed for the WBG top cell under front illumination, because short-wavelength photons were absorbed by the WBG sub-cell before they reach the light-trapping particles at the PEDOT/NBG perovskite interface. The EQE under rear illumination (that is light coming from NBG side) also showed an enhancement in the long wavelength region (Fig. 3d), which is ascribed to the light scattered back from the resin-particle layer. Comparison between the EQE curves and the absorptance and reflectance spectra shows that the improvement in EQE under both front and rear illumination stems from the improvement in absorptance (Fig. 3c-d), which confirms the lighttrapping function of the resin-particle layer. Then, we fabricated bifacial all-perovskite tandem devices using WBG perovskites of different bandgaps (1.65-eV and 1.78-eV) combining with the efficient semitransparent NBG cell with light-trapping structure to demonstrate the benefits of bifacial configuration (Fig. 3e). Despite a large J_{SC} difference between the 1.65-eV WBG top cell and the 1.21-eV NBG bottom cell—19.4 mA/cm² versus 10.9 mA/cm², as calculated from their

respective EQEs—the bifacial tandem device under illumination with 30% of albedo light (backto-front irradiance ratio of 30%) generated an additional photocurrent density of 8.7 mA/cm² in the NBG cell, which balanced the photocurrent from the WBG sub-cell. As a result, the bifacial all-perovskite tandem device fabricated with a 1.65-eV top cell achieved a J_{SC} of 19.4 mA/cm², a V_{OC} of 2.01 V, and an equivalent efficiency of 29.3% under illumination with 30% of albedo light (Fig. 3e), which is confirmed by the steady-state output shown in Fig. 3f. This performance of bifacial all-perovskite tandem device is higher than the equivalent efficiency of ~26.5% for the bifacial single-junction silicon cell under same 30% of albedo light as simulated in our previous study (40). The fill factor was slightly reduced when changing the illumination from mono-facial to bifacial condition due to the increased photocurrent density (Table 1). For the bifacial tandem with a 1.78-eV WBG top cell, the WBG cell limits the J_{SC} of the tandem device to 15.7 mA/cm² (Fig. 3g), with a V_{OC} of 2.05 V and an equivalent efficiency of 24.0% under illumination with 30% of albedo light (Fig. 3e). This efficiency is close to the efficiency of 24.4% for mono-facial tandem counterpart fabricated with a 1.78-eV WBG cell (Fig. 3i and Table 1). More detailed study for the high efficiency mono-facial all perovskite tandem solar cells that we achieved using the similar NBG perovskite and WBG perovskite with matched photocurrent condition could be found in our previous publication (52). For 15 bifacial tandem devices fabricated from the same batch, the mean equivalent efficiency under illumination with 30% of albedo light was increased from 23.3% to 28.3% when the bandgap of top cell changed from 1.78 eV to 1.65 eV (Fig. 3h and Fig. S19). Note that the V_{OC} of the bifacial tandem devices is only reduced by 40 mV when the bandgap of the WBG cell is decreased from 1.78 eV to 1.65 eV (Fig. S19), with a corresponding 90 mV reduction of voltage deficit W_{OC} for the bifacial all-perovskite tandem solar cells.

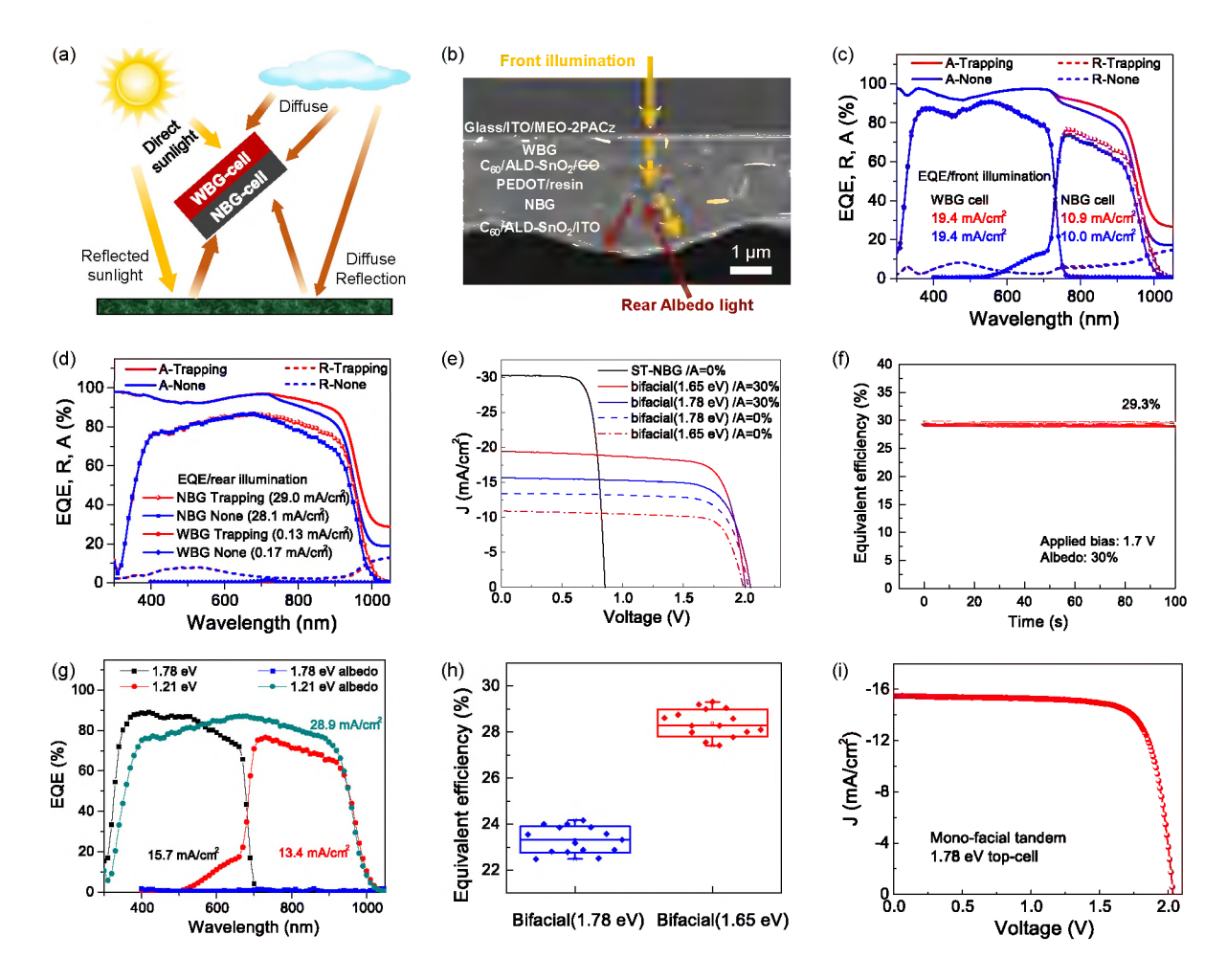


Fig. 3. Performance of bifacial all-perovskite tandem solar cells with embedded light-trapping structure. (a) Sketch of light absorption in a bifacial all-perovskite tandem device with additional albedo light. (b) SEM image of a bifacial all-perovskite tandem device with a light-trapping resinparticle layer at the PEDOT/NBG perovskite interface. EQE, R, and A of bifacial all-perovskite tandem devices (c) under illumination from the front (WBG) side and (d) under illumination from the rear (NBG) side, where the bifacial tandem devices were fabricated with a 1.65-eV WBG top cell and a 1.21-eV NBG bottom cell deposited on neutral PEDOT without and with a light-trapping layer. (e) J–V curves of semi-transparent Pb-Sn cell (ST-NBG), and bifacial tandems fabricated with 1.65-eV and 1.78-eV WBG top cells without (A=0%) and with 30% of albedo light (A=30%). (f) Steady-state output of bifacial tandem with 1.65-eV WBG top cell at the maximum power point

(applied bias of 1.70 V) under illumination with 30% of albedo light. (g) EQE curves of a bifacial all-perovskite tandem device fabricated with a 1.78-eV WBG cell and a 1.21-eV NBG cell with light-trapping layer under front illumination and rear-side albedo light. (h) equivalent efficiency distribution of 15 bifacial tandems fabricated in same batch with 1.78-eV and 1.65-eV WBG top cells under illumination with 30% of albedo light, where the box indicates the standard deviation and the line inside box represents the mean value. (i) J–V curve of a mono-facial all-perovskite tandem solar cell fabricated with a 1.78-eV WBG top cell and a 1.21-eV NBG bottom cell.

Table 1. Photovoltaic performance of bifacial and mono-facial devices. Summary of photovoltaic parameters for semitransparent 1.21 eV Pb-Sn cell (ST-NBG), bifacial tandems fabricated with 1.65-eV and 1.78-eV WBG top cells without (A=0%) and with 30% of albedo light (A=30%), and mono-facial tandem with 1.78-eV WBG top cell.

Device	Voc (V)	J _{SC} (mA/cm ²)	FF (%)	η (%)
ST-NBG/A=0%	0.85	30.2	76.4	19.6
Bifacial (1.65 eV) /A=30%	2.01	19.4	75.0	29.3
Bifacial (1.78 eV) /A=30%	2.05	15.7	74.7	24.0
Bifacial (1.65 eV) /A=0%	1.99	10.9	76.8	16.7
Bifacial (1.78 eV) /A=0%	2.03	13.4	76.0	20.6
Mono-facial (1.78 eV)	2.03	15.4	78.1	24.4

Energy-yield simulations

We simulated the energy yield of bifacial all-perovskite tandem solar cells and their monofacial counterparts to illustrate the benefits of bifacial configuration, as shown in Fig. 4. The

installation parameters—such as ground cover, use of tracking, ground clearance, row spacing, and location—can be used (to some extent) to tailor the effective albedo for the applications of bifacial all-perovskite tandem devices (40). For example, annual average effective albedos of 25% and 34% can be achieved in Phoenix (Arizona, USA) with white sand as the ground surface using single-axis tracking and fixed-tilt systems, respectively; these effective albedo values are reduced to 10% and 13%, respectively, when assuming the exact same system configurations on brown loam ground, which presents a lower surface albedo (Fig. S20). Fig. 4a and 4b show the relation between the annual energy yield and the bandgap of the WBG top cell for mono-facial and bifacial tandem modules installed in Phoenix on white sand or brown loam in single-axis-tracking (Fig. 4a) or fixed-tilt (Fig. 4b) systems. As expected, higher average effective albedos reduce the optimal bandgap of the WBG top cell and boost the energy yield in a wide range of top-cell bandgaps when compared with mono-facial tandem devices (40-43). That is, bifaciality relaxes the constraint on the bandgap of the WBG top cell. For instance, with single-axis tracking on white sand in Phoenix, the maximum annual energy yield could be increased from 879 kWh/m² for mono-facial tandem modules with a 1.78-eV WBG top cell to 983 kWh/m² for bifacial tandem modules with a 1.65eV WBG top cell (Fig. 4a), an 11.8% increase of the energy yield. For bifacial tandem modules with single-axis on brown loam, the increase in energy yield is more limited, with an improvement of 5.5% from 870 kWh/m² to 918 kWh/m² when switching from mono-facial with a 1.78-eV WBG cell to bifacial with an optimal 1.73-eV WBG cell (Fig. 4a). The effect of the WBG-cell voltage deficit W_{OC} on the annual energy yield under different effective albedo conditions is presented in Fig. 4c-f. Fig. S21 and Table S1 summarize the W_{OC} of reported high-V_{OC} WBG perovskite solar cells (53) and Fig. S21 also shows the W_{OC} model we used in our simulations, where our W_{OC} model assumes a reduction of W_{OC} when decreasing the bandgap of the WBG cell. Fig. 4c shows

that, in Phoenix on white sand with single-axis tracking, if W_{OC} of 1.78 eV WBG cells is reduced by 90 mV—from 0.57 V to 0.48 V—the annual energy yield of corresponding bifacial tandem devices will improve by 5.2%, from 882 kWh/m² to 928 kWh/m². Therefore, bifacial all-perovskite tandem solar cells not only harvest additional albedo light to increase the energy yield, but also decrease the optimal bandgap of the WBG cell, opening the way to using cells with lower W_{OC} and, thus, allowing a further increase in energy yield. As crystalline silicon PV panels are shifting to bifacials, there are albedo-enhancing technologies being deployed to increase energy yield.

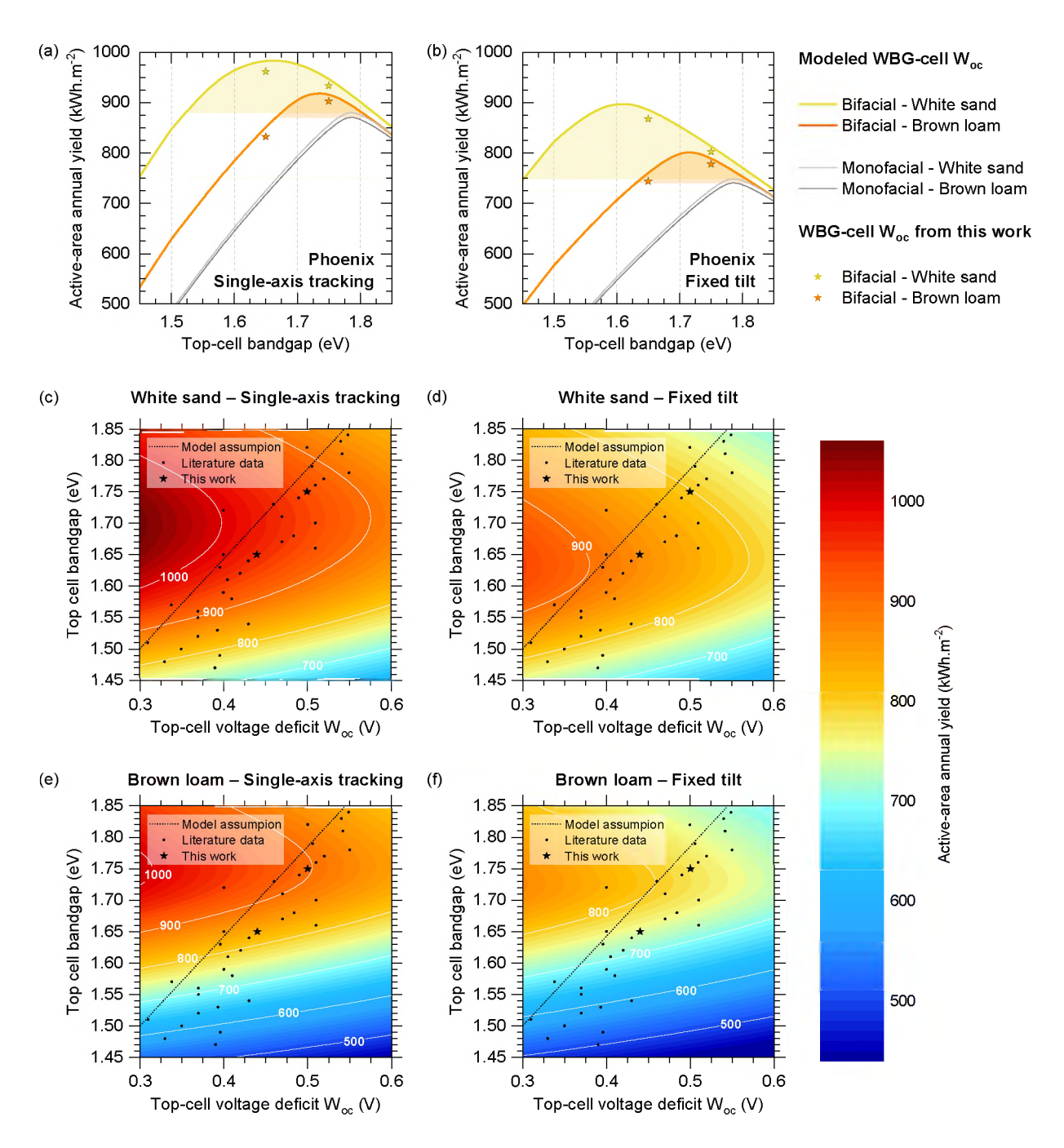


Fig. 4. Energy-yield simulations for bifacial all-perovskite tandem solar modules. Simulated annual energy yield of bifacial and mono-facial all-perovskite tandem solar modules installed on white sand and brown loam in Phoenix, AZ with (a) single-axis-tracking and (b) fixed-tilt systems. The modeled relation between the bandgap of the WBG-cell and its voltage deficit W_{OC} is based on the best WBG-cell reported in the Perovskite Database, as detailed in the Supplementary

Information. Note that, as opposed to our WBG-cell, these best WBG-cells are not necessarily semi-transparent or process-compatible with integration into a tandem device. Hence, our devices—on which the constraint are substantially stronger—present a slightly larger W_{OC} than assumed in the model. The shaded areas represent the ranges of WBG-top-cell bandgaps for which bifacial tandem modules outperform their optimized mono-facial counterparts. Calculated annual yield of bifacial all-perovskite tandem solar modules with different WBG-top-cell bandgaps and voltage deficits W_{OC} installed in Phoenix, AZ on (c and d) white sand and (e and f) brown loam with single-axis tracking (c and e) and fixed tilt (d and f). The dots represent the WBG-top-cell bandgaps and W_{OC} of the best cells reported in the literature, the dashed line represent the bandgap— W_{OC} relation we have assumed in the simulations shown in Fig. 4a and 4b.

For the energy yield simulation result in Fig. 4, the impact of temperature and dead areas were not included. The impact of temperature on the performance of the modules was ignored in here for two reasons: 1) experimentally validated temperature coefficients for the NBG- and WBG-cells were not available, and 2) a custom thermal model specific to thin-film all-perovskite tandem modules would have to be built, for which the parameters are unknown and dependent on design and technology choices that are yet to be made. Consequently, building a specific thermal model implies assumptions that go beyond the scope of the current publication. However, we assume that the thermal coefficients of the NBG- and WBG-cells are of the same sign—as opposed to perovskite/silicon tandem modules (54)—so temperature effects should have a minimal impact on current matching between the sub-cells. So far, there is no standard geometric fill factor to reference for perovskite modules, how bifacial all-perovskite tandems will be implemented at the commercial scale still need to be found out, therefore, we reported active-area power densities in

Fig. 4 a and b without considering the dead areas (scribe-lines, module frame, etc.) of the module. A geometric fill factor must be assumed to translate these numbers into "full-module" numbers, and adding such a constant geometric fill factor across all modules would only decrease the absolute energy yield but not change the shape of the curves in Fig. 4. Thus, our main conclusions remain unchanged regarding the optimal bandgap for the WBG-cell.

For the cost estimation of photovoltaic module, the difference between mono-facial and bifacial tandem devices is the change from thermal evaporated BCP/Cu to sputtered ITO electrode with SnO₂ buffer layer. Based on the cost estimation by Li *et al.* and Chang *et al.* (4,55), the cost of thermal evaporated BCP/Cu electrode is ~\$2/m² among the total cost of \$45.23/m² for all-perovskite tandem solar cells, and the estimated cost of SnO₂ buffer layer and sputtered ITO electrode is \$0.57/m² and \$1.77/m², respectively (4,55). This shows that there will be less than 1% of cost changes between mono-facial and bifacial all-perovskite tandem solar cells, while the efficiency gain can be as large as 10% based on the energy-yield simulations. Therefore, the bifacial all-perovskite tandem solar cells will be attractive for the solar energy harvesting.

DISCUSSION

In summary, we report the fabrication of efficient bifacial all-perovskite tandem solar cells based on enhanced narrow-bandgap Pb-Sn perovskite sub-cells with an embedded light-scattering layer and non-acidic HTL. We develop a resin-particle based light-trapping layer to increase the photon pathlength in semitransparent Pb-Sn perovskite solar cells and replace the acidic PEDOT:PSS hole transport layer with neutral PEDOT for better thermal stability to achieve efficient charge collection. As a result, the efficiency of semitransparent Pb-Sn perovskite solar cells is boosted from 15.6% to 19.4%, which benefits the performance of bifacial all-perovskite

tandem solar cells. With 30% of albedo light, bifacial all-perovskite tandem solar cells could use 1.65 eV perovskite instead of 1.78 eV perovskite as WBG sub-cells. As a result, 1.78-eV perovskite cells—which exhibit large voltage deficit W_{OC} —can be avoided, and, using a 1.65-eV WBG cell instead, the W_{OC} of tandem device is reduced, leading to an equivalent efficiency of 29.3% under 30% of albedo light.

MATERIALS AND METHODS

Materials. PbI₂ (99.999%), PbBr₂ (99.999%), SnI₂ (99.999%), CsI (99.999%), barium iodide (BaI₂, 99.995%), rubidium iodide (RbI, 99.9%), bathocuproine (BCP), tris(pentafluorophenyl)borane (95%), choline chloride (\geq 98%), 1,4-Diaminobutane (BDA, 99%), methylamine solution (33 wt.% in absolute ethanol), N,N-dimethylformamide (DMF, anhydrous, 99.8%), dimethyl sulfoxide (DMSO, anhydrous, 99.8%), toluene (anhydrous, 99.8%), isopropyl alcohol (anhydrous, 99.5%), ethyl acetate (anhydrous, 99.8%), sulfonic acid cation exchange resins (Amberlyst 15, hydrogen form) were purchased from Sigma-Aldrich. MEO-2PACz (>98%) was purchased from TCI. PEDOT:PSS (Clevios™ P VP AI 4083) and PEDOT (HTL Solar 3) were purchased from Ossila. Formamidinium iodide (FAI), phenethylammonium bromide (PEABr), and phenethylammonium chloride (PEACl) were purchased from GreatCell Solar. C₆₀ was purchased from Nano-C Inc. Aqueous single-layer graphene-oxide (GO) solution with concentration of 500 mg/L was purchased from Graphene Supermarket. MAPbCl₃ single crystals were synthesized using a previously reported method (56). Copper (Cu) pellets and the indium tin oxide (ITO) target were purchased from Kurt J. Lesker Company. Polytetrafluoroethylene (PTFE) and Nylon filters were purchased from VWR.

Preparation of precursor solutions.

Pb-Sn perovskite precursor solution: 2.0 M Cs_{0.2}FA_{0.8}Pb_{0.5}Sn_{0.5}I₃ (1.21 eV) Pb-Sn perovskite solution was prepared by dissolving 0.41 M CsI, 1.64 M FAI, 1.0 M PbI₂, 1.0 M SnI₂ and 0.1 M SnF₂ in mixed solvent of DMSO and DMF with a volume ratio of 1:3. After stirring at room temperature in N₂-filled gloveboxes overnight, 2.5 mg/ml PEACl, 0.78 mg/ml BaI₂, and 0.42 mg/ml RbI were added into the precursor solution. The perovskite precursor solution was filtered with 0.22-μm PTFE filter before use.

WBG perovskite precursor solutions: 1.35 M Cs_{0.4}FA_{0.6}PbI_{2.04}Br_{0.96} (1.78 eV) precursor solution was prepared by dissolving 0.54 M CsI, 0.81 M FAI, 0.648 M PbBr₂, 0.702 M PbI₂, 0.054M MAPbCl₃ single crystals, and 1.0 mg/ml PEABr in mixed solvent of DMSO and DMF with a volume ratio of 3:7 and stirred at room temperature in gloveboxes overnight. 1.65 eV perovskite precursor was prepared by mixing 1.78 eV perovskite precursor with FAPbI₃ precursor (1.8 M in mixed solvent of DMSO and DMF with volume ratio of 3:7) at volume ratio of 1:0.6.

PEDOT:PSS solution: Commercial Clevios™ P VP AI 4083 solution (pH value of 1-2) was filtered with 0.22-µm Nylon filter before use.

PEDOT solution: HTL Solar 3 solution (pH value of ~2, without PSS ionomer) was mixed with tris(pentafluorophenyl)borane solution (2.6 mg/mL in toluene) at volume ratio of 1:1 and was filtered with 0.22-µm PTFE filter before use.

Resin particle suspension: Commercial cation exchange resins Amberlyst 15 were first mixed with high-concentration NaOH aqueous solution under stirring to convert from hydrogen form to sodium form. After washing with deionized water and drying in an oven, the sodium-form cation-exchange resins were finely powdered in isopropyl alcohol using a 130-W ultrasonic processor for 4 hours. This suspension solution was used for deposition of resin-particle layers.

Pb-Sn perovskite solar cells fabrication. Patterned ITO/glass substrates were sequentially cleaned in deionized water, acetone, and isopropyl alcohol with ultrasonication for 30 min, and then UV-ozone treated for 15 min before use. Acidic PEDOT:PSS hole transport layers were coated onto ITO/glass substrate by spin-coating the PEDOT:PSS solution at 5000 r.p.m for 30 s and annealing at 150 °C for 15 min in ambient condition. Neutral PEDOT hole transport layers were coated onto ITO/glass substrate by spin-coating the PEDOT solution at 6000 r.p.m for 30 s, annealing at 150 °C for 15 min in N₂-filled glovebox, and spin-coating the films with 0.4 wt% methylamine in ethanol at 5000 r.p.m for 30 s to neutralize the PEDOT layer. Acidic PEDOT hole transport layers were obtained by spin-coating the PEDOT solution at 6000 r.p.m for 30 s and annealing at 150 °C for 15 min in N₂-filled glovebox. The resin-particle layers were deposited by spin-coating the resin-particle suspension solution at 2500 r.p.m for 30 s twice and annealing at 100 °C for 5 min. Then, the NBG perovskite precursor solution was spin-coated at 1500 r.p.m for 18 s and 3500 r.p.m for 45 s, 0.13 mL of ethyl acetate was quickly dropped onto the spinning substrate after 55 s elapsed, followed by annealing at 130 °C for 7 min. For surface passivation, a 0.02 mM BDA solution in toluene was dropped onto the perovskite films during spin-coating at 5000 r.p.m for 30 s followed by annealing at 70 °C for 5 min. The devices with C₆₀/BCP/Cu electron transport layers and electrodes were finished by sequentially depositing C₆₀ (20 nm), BCP (8 nm), and Cu (90 nm) on the perovskite film by thermal evaporation. For the devices with C₆₀/ALD-SnO₂/Cu stack, 20 nm of C₆₀ were first thermally evaporated, followed with deposition of 15 nm of SnO₂ through 210 ALD cycles at 85 °C for 150 min in a Cambridge NanoTech Savannah G2 tool, and finished with thermal evaporation of a 90-nm-thick Cu electrode. The devices with C₆₀/ALD-SnO₂/ITO were finished with a 80-nm-thick ITO

electrode, which was on top of the SnO₂ buffer layer sputtered from a 4-inch ITO target at a power of 100 W in a Kurt J. Lesker PVD 75 Pro Line tool under argon atmosphere with 0.4% of oxygen. A pyramidally textured polydimethylsiloxane (PDMS) layer was added to the glass surface to reduce the reflection (57). The device areas of Pb-Sn solar cells were 8 mm².

Bifacial all-perovskite tandem solar cells fabrication. The bifacial all-perovskite tandem solar cells were fabricated with the stack of following layers: glass (700 µm)/ITO (120 nm)/MEO-2PACz (monolayer)/WBG (540 nm)/C₆₀ (20 nm)/SnO₂ (15 nm)/graphene-oxide (<5 nm)/PEDOT (30 nm)/resin (~1000 nm)/NBG (1200 nm)/C₆₀ (20 nm)/SnO₂ (15 nm)/ITO (80 nm). 2 mM MEO-2PACz in isopropyl alcohol was spin-coated at 6000 r.p.m for 20 s onto UV-ozone treated ITO/glass substrates and annealed at 100 °C for 30 min. Then, the WBG perovskite precursor solution was spin-coated onto the MEO-2PACz HTL at 3000 r.p.m for 30 s. After spin-coating, N₂ was blown on the film for 40 s using an N₂ gun, the film was then annealed at 65 °C for 1 min and 105 °C for 20 min. Then, 1 mg/ml PEABr in isopropyl alcohol was spin-coated onto the annealed perovskite film followed with annealing at 100 °C for 10 min. Subsequently, 1 mg/ml choline chloride in isopropyl alcohol was spin-coated onto the perovskite film, followed by annealing at 100 °C for 20 min. Next, 20 nm of C₆₀ were thermally evaporated, and 15 nm of SnO₂ were deposited through 210 cycles ALD at 85 °C. After ALD deposition, the as-purchased graphene-oxide solution was spin-coated on the top of ALD-SnO₂ followed by annealing at 105 °C for 30 min to get a less than 5 nm of recombination layer. Neutral PEDOT, resin-particle layer, Pb-Sn NBG perovskite, C₆₀, ALD-SnO₂, and sputtered ITO electrode were deposited by the same procedures as the single-junction semi-transparent NBG perovskite solar cells. Pyramidally

textured PDMS layers were added to both surfaces of device to reduce the reflection. The device areas of bifacial all-perovskite tandem solar cells were 8 mm².

Characterization. Current-voltage (J-V) measurements were performed using a Keithley 2400 source meter at a scan rate of 0.1 V·s⁻¹ under AM1.5G illumination (100 mW/cm²), which was produced by a Xenon-lamp-based solar simulator (94043A, Newport Sol3ATM Class AAA). The light intensity was calibrated using a 91150-KG5 silicon reference cell mounted with a KG5 window. J-V measurements with albedo light were performed under illumination from both the front side and the rear side, with the cell's front side illuminated at 1-sun-equivalent using a Xenon-lamp-based solar simulator (Oriel 67005) whereas the cell's rear side was illuminated by a separate Xenon-lamp-based solar simulator (94043A) equipped with an integrated partial-sun attenuator to tune the intensity of rear illumination to 0.3-sun-equivalent. EQE measurements were conducted with a Newport QE measurement kit, by focusing a monochromatic light beam from a Xenon Arc lamp coupled with a Bruker Vertex 80v Fourier Transform Interferometer onto the devices. Then the photocurrent was obtained through Stanford Research SR570 current preamplifier. EQE of devices were calibrated by a Newport reference silicon solar cell with a known EQE. In tandem devices, the EQEs of the WBG sub-cells and the NBG sub-cells were measured under infrared bias light (~940 nm) and blue bias light (~470 nm) at an equivalent intensity of ~0.3 sun, respectively. X-ray diffraction (XRD) patterns were acquired with a Rigaku Miniflex 6GBenchtop XRD system. GIXRD measurements were carried out with a Rigaku SmartLab diffractometer using Cu Ka radiation, and the height of films was calibrated before each measurement. For the characterization of the reaction products of Pb-Sn perovskite films under thermal stress, Pb-Sn perovskite films deposited on varying HTLs and on bare

ITO/glass were soaked in 8 mL toluene in sealed 50 mL vials inside N₂-filled gloveboxes. After annealing on 100 °C hot plate with temperature of toluene solution at 85 °C for 48 hours, the extracted reaction products in toluene were characterized through absorptance measurement by PerkinElmer LAMBDA 1050+ UV/Vis/NIR spectrophotometers. I₂ vapor treatment was carried out by sealing the perovskite films with ~0.1 g of I₂ powder in 20 mL vials inside N₂-filled gloveboxes in the dark. The I₂ powder was sublimated into I₂ vapor, which reached and reacted with the perovskite films. After I₂ vapor treatment, the samples were taken out of the vials and annealed at 50 °C in N₂-filled gloveboxes for 3 min in order to sublimate the adsorbed I₂. The reaction products were then extracted by soaking the films in 4 mL toluene for absorptance measurement by PerkinElmer spectrophotometers. Scanning electron microscopy (SEM) images were taken with a FEI Helios 600 Nanolab tool. Transient photovoltage (TPV) decays were measured under 1-sun illumination, using a 337-nm laser pulse (SRS NL 100 Nitrogen Laser, pulse duration of less than 3.5 ns) to add a small perturbation to the background illumination. The voltage of the device was measured with a digital oscilloscope (DOS-X 3104A) with an input impedance set to 1 M Ω . For TPC measurement, the device was connected to the oscilloscope with an input impedance set to 50 Ω to form a short-circuit condition, and the photocurrent variation (ΔI) was created by the 337-nm laser pulse (SRS NL 100 Nitrogen Laser) under dark condition. The device size for TPC measurement was reduced by scribing with a knife to reduce the capacitor to <100 pF for a RC constant of <5 ns. Haze characterization was performed with a Lambda 950 UV-VIS spectrophotometer from PerkinElmer that equipped with a 150 mm integrating sphere. We measured the diffuse transmittance and total transmittance of the sample, respectively, and calculated the Haze by the ratio of the two spectra. Annual energy yield simulations. Annual energy yield simulations were carried out by combining results from the software SunSolve™ from PV Lighthouse—used to obtain the front and back irradiances (in suns-equivalent) on bifacial modules—with a bifacial tandem device model developed in-house (40). For the four power-plant configurations considered (fixed-tilt on brown loam, single-axis tracking on brown loam, fixed-tilt on white sand, single-axis tracking on white sand), we used the SunSolveTM Yield tool to determine the photo-generated current densities from front and rear irradiance over the course of a model year in the case of bifacial silicon PERC modules. We simulated unit PV systems with either single-axis tracking or fixed tilt configuration located in Phoenix, AZ. The unit system consists of a single module (977 cm x 1958 cm) in portrait orientation mounted on a 12.5-cm-diameter torque tube that is 1.6 meters above the ground. It presents a full system with a module row pitch of 5.5 meters and 2 cm gap between modules in the same row. In the single-axis-tracking case, rows are oriented north-south, with a max tilt angle of $\pm 60^{\circ}$ and back-tracking implemented. In the fixed-tilt case, rows are oriented east-west with a tilt of 29°. Spectrally resolved albedos for brown loam and white sand were extracted from the ASTER database (58) and used as inputs in SunSolve, assuming reflection off the ground surface to be lambertian. For each hour of the year, we extracted the front and rear photo-generated current densities for standard PERC modules and, knowing the front and rear J_{SC} of these PERC modules under AM1.5G illumination (direct illumination for the front J_{SC}, diffuse illumination for the rear J_{SC}), we converted the hour-per-hour front and rear photo-generated currents into irradiances (direct on the front, diffuse on the rear) in numbers of suns-equivalent.

These hour-per-hour front and rear irradiances (in suns-equivalent) were used as inputs for our bifacial tandem device model. This model is adapted from the earlier work from Onno *et al.* on perovskite/silicon bifacial tandem devices (40). To ensure that the total front EQE of modeled

all-perovskite bifacial tandem modules is independent of the WBG-cell bandgap, we assumed that both perovskite layers were conformally deposited on textured glass. Thus, we minimized interferences at the band-edge of the WBG cell. We used the spectrally resolved complex refractive indices of 1.65-eV WBG and 1.21-eV NBG perovskites—determined by ellipsometry and spectrophotometry—as inputs in the SunSolveTM Power tool to calculate the front (direct illumination) and rear (diffuse illumination) total EQEs of the assumed all-perovskite bifacial tandem module, and confirmed that both EQEs were independent of the WBG-cell bandgap. Similar to the technique used by Onno et al. (40) (itself inspired by previous work from Manzoor et al. (59)), for arbitrary WBG-cell bandgaps, we reconstructed the front WBG- and NBG-cell EQEs from the total front EQE by shifting the absorptance of the WBG cell. For each hour of the year, we calculated the photo-generated currents in both sub-cells from the reconstructed front and rear WBG- and NBG-cell EQEs and from the irradiances (in suns-equivalent) extracted from SunSolveTM, assuming a spectral irradiance equal to AM1.5G scaled by the number of sunsequivalent. The underlying assumption is that the all-perovskite tandem modules present an angular sensitivity similar to that of the bifacial PERC modules simulated in SunSolve™ Yield. Hourly resolved J-V curves were then calculated for each sub-cell, using one-diode models for both sub-cells. For each WBG-cell bandgap, the equilibrium recombination current of the WBGcell was adjusted to match the assumed Voc deficit. The equilibrium recombination current of the 1.21-eV NBG-cell was adjusted to match the V_{OC} reported in **Table 1**. For each hour of the day, the tandem module yield was then computed by finding the maximum power point with the constraint of current matching between the WBG and NBG cells, assuming a total series resistance of 15 Ω .cm².

REFERENCES AND NOTES

- 1. X. Zheng, A. Y. Alsalloum, Y. Hou, E. H. Sargent, O. M. Bakr. All-perovskite tandem solar cells: A roadmap to uniting high efficiency with high stability. *Acc. Mater. Res.* 1, 63-76 (2020).
- 2. M. T. Hörantner, T. Leijtens, M. E. Ziffer, G. E. Eperon, M. G. Christoforo, M. D. McGehee, H. J. Snaith. The potential of multijunction perovskite solar cells. *ACS Energy Lett.* **2**, 2506-2513 (2017).
- 3. T. Leijtens, K. A. Bush, R. Prasanna, M. D. McGehee. Opportunities and challenges for tandem solar cells using metal halide perovskite semiconductors. *Nat. Energy* **3**, 828-838 (2018).
- 4. Z. Li, Y. Zhao, X. Wang, Y. Sun, Z. Zhao, Y. Li, H. Zhou, Q. Chen. Cost analysis of perovskite tandem photovoltaics. *Joule* **2**, 1559-1572 (2018).
- 5. J. H. Heo, J. H. Im. CH₃NH₃PbBr₃-CH₃NH₃PbI₃ perovskite-perovskite tandem solar cells with exceeding 2.2 V open circuit voltage. *Adv. Mater.* **28**, 5121-5125 (2016).
- 6. G. E. Eperon, T. Leijtens, K. A. Bush, R. Prasanna, T. Green, J. T. W. Wang, D. P. McMeekin, G. Volonakis, R. L. Milot, R. May, A. Palmstrom, D. J. Slotcavage, R. A. Belisle, J. B. Patel, E. S. Parrott, R. J. Sutton, W. Ma, F. Moghadam, B. Conings, A. Babayigit, H. G. Boyen, S. Bent, F. Giustino, L. M. Herz, M. B. Johnston, M. D. McGehee, H. J. Snaith. Perovskite-perovskite tandem photovoltaics with optimized band gaps. *Science* 354, 861-865 (2016).
- 7. Z. Yang, A. Rajagopal, C.-C. Chueh, S. B. Jo, B. Liu, T. Zhao, A. K.-Y. Jen. Stable low-bandgap Pb–Sn binary perovskites for tandem solar cells. *Adv. Mater.* **28**, 8990-8997 (2016).
- 8. D. Zhao, C. Chen, C. Wang, M. M. Junda, Z. Song, C. R. Grice, Y. Yu, C. Li, B. Subedi, N. J. Podraza, X. Zhao, G. Fang, R.-G. Xiong, K. Zhu, Y. Yan. Efficient two-terminal all-perovskite tandem solar cells enabled by high-quality low-bandgap absorber layers. *Nat. Energy* 3, 1093-1100 (2018).
- A. F. Palmstrom, G. E. Eperon, T. Leijtens, R. Prasanna, S. N. Habisreutinger, W. Nemeth, E. A. Gaulding, S. P. Dunfield, M. Reese, S. Nanayakkara, T. Moot, J. Werner, J. Liu, B. To, S. T. Christensen, M. D. McGehee, M. van Hest, J. M. Luther, J. J. Berry, D. T. Moore. Enabling flexible all-perovskite tandem solar cells. *Joule* 3, 2193-2204 (2019).

- 10. Z. Yang, Z. Yu, H. Wei, X. Xiao, N. Zhenyi, B. Chen, Y. Deng, S. N. Habisreutinger, X. Chen, K. Wang, J. Zhao, P. N. Rudd, J. J. Berry, M. C. Beard, J. Huang. Enhancing electron diffusion length in narrow-bandgap perovskites for efficient monolithic perovskite tandem solar cells. *Nat. Commun.* 10, 4498 (2019).
- J. H. Tong, Z. N. Song, D. H. Kim, X. H. Chen, C. Chen, A. F. Palmstrom, P. F. Ndione, M. O. Reese, S. P. Dunfield, O. G. Reid, J. Liu, F. Zhang, S. P. Harvey, Z. Li, S. T. Christensen, G. Teeter, D. W. Zhao, M. M. Al-Jassim, M. van Hest, M. C. Beard, S. E. Shaheen, J. J. Berry, Y. F. Yan, K. Zhu. Carrier lifetimes of > 1 μs in Sn-Pb perovskites enable efficient all-perovskite tandem solar cells. *Science* 364, 475-479 (2019).
- 12. R. Lin, K. Xiao, Z. Qin, Q. Han, C. Zhang, M. Wei, M. I. Saidaminov, Y. Gao, J. Xu, M. Xiao, A. Li, J. Zhu, E. H. Sargent, H. Tan. Monolithic all-perovskite tandem solar cells with 24.8% efficiency exploiting comproportionation to suppress Sn (II) oxidation in precursor ink. *Nat. Energy* 4, 864-873 (2019).
- 13. Z. Yu, Z. Yang, Z. Ni, Y. Shao, B. Chen, Y. Lin, H. Wei, J. Huang. Simplified interconnection structure for efficient and stable all-perovskite tandem solar cells. *Nat. Energy* **5**, 657-665 (2020).
- 14. K. Xiao, R. Lin, Q. Han, Y. Hou, Z. Qin, H. T. Nguyen, J. Wen, M. Wei, V. Yeddu, M. I. Saidaminov, Y. Gao, X. Luo, Y. Wang, H. Gao, C. Zhang, J. Xu, J. Zhu, E. H. Sargent, H. Tan. All-perovskite tandem solar cells with 24.2% certified efficiency and area over 1 cm² using surface-anchoring zwitterionic antioxidant. *Nat. Energy* 5, 870-880 (2020).
- 15. C. Li, Z. Song, C. Chen, C. Xiao, B. Subedi, S. P. Harvey, N. Shrestha, K. K. Subedi, L. Chen, D. Liu, Y. Li, Y.-W. Kim, C.-s. Jiang, M. J. Heben, D. Zhao, R. J. Ellingson, N. J. Podraza, M. Al-Jassim, Y. Yan. Low-bandgap mixed tin–lead iodide perovskites with reduced methylammonium for simultaneous enhancement of solar cell efficiency and stability. *Nat. Energy* 5, 768-776 (2020).
- R. Lin, J. Xu, M. Wei, Y. Wang, Z. Qin, Z. Liu, J. Wu, K. Xiao, B. Chen, S. M. Park, G. Chen, H.
 R. Atapattu, K. R. Graham, J. Zhu, L. Li, C. Zhang, E. H. Sargent, H. Tan. All-perovskite tandem solar cells with improved grain surface passivation. *Nature* 603, 73-78 (2022).

- 17. J. Tong, Q. Jiang, A. J. Ferguson, A. F. Palmstrom, X. Wang, J. Hao, S. P. Dunfield, A. E. Louks, S. P. Harvey, C. Li, H. Lu, R. M. France, S. A. Johnson, F. Zhang, M. Yang, J. F. Geisz, M. D. McGehee, M. C. Beard, Y. Yan, D. Kuciauskas, J. J. Berry, K. Zhu. Carrier control in Sn-Pb perovskites via 2D cation engineering for all-perovskite tandem solar cells with improved efficiency and stability. *Nat. Energy* 7, 642-651 (2022).
- M. A. Green, E. D. Dunlop, J. Hohl-Ebinger, M. Yoshita, N. Kopidakis, K. Bothe, D. Hinken, M. Rauer, X. Hao. Solar cell efficiency tables (Version 60). *Prog. Photovolt.: Res. Appl.* 30, 687-701 (2022).
- Z. F. Liu, L. Kruckemeier, B. Krogmeier, B. Klingebiel, J. A. Marquez, S. Levcenko, S. Oz, S. Mathur, U. Rau, T. Unold, T. Kirchartz. Open-circuit voltages exceeding 1.26 V in planar methylammonium lead iodide perovskite solar cells. ACS Energy Lett. 4, 110-117 (2019).
- S. Chen, Y. Hou, H. W. Chen, X. F. Tang, S. Langner, N. Li, T. Stubhan, I. Levchuk, E. Gu, A. Osvet, C. J. Brabec. Exploring the stability of novel wide bandgap perovskites by a robot based high throughput approach. *Adv. Energy Mater.* 8, 1701543 (2018).
- S. Gharibzadeh, B. A. Nejand, M. Jakoby, T. Abzieher, D. Hauschild, S. Moghadamzadeh, J. A. Schwenzer, P. Brenner, R. Schmager, A. A. Haghighirad, L. Weinhardt, U. Lemmer, B. S. Richards, I. A. Howard, U. W. Paetzold. Record open-circuit voltage wide-bandgap perovskite solar cells utilizing 2D/3D perovskite heterostructure. *Adv. Energy Mater.* 9, 1803699 (2019).
- Y. Zhou, Y. H. Jia, H. H. Fang, M. A. Loi, F. Y. Xie, L. Gong, M. C. Qin, X. H. Lu, C. P. Wong,
 N. Zhao. Composition-tuned wide bandgap perovskites: from grain engineering to stability and
 performance improvement. Adv. Funct. Mater. 28, 1803130 (2018).
- J. P. Correa-Baena, W. Tress, K. Domanski, E. H. Anaraki, S. H. Turren-Cruz, B. Roose, P. P. Boix, M. Gratzel, M. Saliba, A. Abate, A. Hagfeldt. Identifying and suppressing interfacial recombination to achieve high open-circuit voltage in perovskite solar cells. *Energy Environ. Sci.* 10, 1207-1212 (2017).

- Z. P. Wang, Q. Q. Lin, F. P. Chmiel, N. Sakai, L. M. Herz, H. J. Snaith. Efficient ambient-air-stable solar cells with 2D-3D heterostructured butylammonium-caesium-formamidinium lead halide perovskites. *Nat. Energy* 2, 17135 (2017).
- M. Abdi-Jalebi, Z. Andaji-Garmaroudi, S. Cacovich, C. Stavrakas, B. Philippe, J. M. Richter, M. Alsari, E. P. Booker, E. M. Hutter, A. J. Pearson, S. Lilliu, T. J. Savenije, H. Rensmo, G. Divitini, C. Ducati, R. H. Friend, S. D. Stranks. Maximizing and stabilizing luminescence from halide perovskites with potassium passivation. *Nature* 555, 497-501 (2018).
- S. Gharibzadeh, B. Abdollahi Nejand, M. Jakoby, T. Abzieher, D. Hauschild, S. Moghadamzadeh,
 J. A. Schwenzer, P. Brenner, R. Schmager, A. A. Haghighirad. Record Open-Circuit Voltage Wide-Bandgap Perovskite Solar Cells Utilizing 2D/3D Perovskite Heterostructure. *Adv. Energy Mater.* 9, 1803699 (2019).
- D. Kim, H. J. Jung, I. J. Park, B. W. Larson, S. P. Dunfield, C. Xiao, J. Kim, J. Tong, P. Boonmongkolras, S. G. Ji. Efficient, stable silicon tandem cells enabled by anion-engineered wide-bandgap perovskites. *Science* 368, 155-160 (2020).
- Q. F. Ye, F. Ma, Y. Zhao, S. Q. Yu, Z. M. Chu, P. Q. Gao, X. W. Zhang, J. B. You. Stabilizing γ-CsPbI₃ perovskite via phenylethylammonium for efficient solar cells with open-circuit voltage over 1.3 V. Small 16 (2020).
- Y. Yu, C. Wang, C. R. Grice, N. Shrestha, D. Zhao, W. Liao, L. Guan, R. A. Awni, W. Meng, A. J. Cimaroli. Synergistic effects of lead thiocyanate additive and solvent annealing on the performance of wide-bandgap perovskite solar cells. ACS Energy Lett. 2, 1177-1182 (2017).
- 30. M. Stolterfoht, C. M. Wolff, J. A. Márquez, S. Zhang, C. J. Hages, D. Rothhardt, S. Albrecht, P. L. Burn, P. Meredith, T. Unold. Visualization and suppression of interfacial recombination for higherficiency large-area pin perovskite solar cells. *Nat. Energy* 3, 847-854 (2018).
- J. Xu, C. C. Boyd, J. Y. Zhengshan, A. F. Palmstrom, D. J. Witter, B. W. Larson, R. M. France, J. Werner, S. P. Harvey, E. J. Wolf. Triple-halide wide-band gap perovskites with suppressed phase segregation for efficient tandems. *Science* 367, 1097-1104 (2020).

- 32. S. Yang, J. Dai, Z. Yu, Y. Shao, Y. Zhou, X. Xiao, X. C. Zeng, J. Huang. Tailoring passivation molecular structures for extremely small open circuit voltage loss in perovskite solar cells. *J. Am. Chem. Soc.* **141**, 5781-5787 (2019).
- W. Q. Wu, P. N. Rudd, Q. Wang, Z. Yang, J. Huang. Blading phase-pure formamidinium-alloyed perovskites for high-efficiency solar cells with low photovoltage deficit and improved stability. *Adv. Mater.*, 2000995 (2020).
- 34. W.-Q. Wu, P. N. Rudd, Z. Ni, C. H. Van Brackle, H. Wei, Q. Wang, B. R. Ecker, Y. Gao, J. Huang. Reducing surface halide deficiency for efficient and stable iodide-based perovskite solar cells. *J. Am. Chem. Soc.* **142**, 3989-3996 (2020).
- 35. D. J. Slotcavage, H. I. Karunadasa, M. D. McGehee. Light-induced phase segregation in halide-perovskite absorbers. *ACS Energy Lett.* **1**, 1199-1205 (2016).
- 36. S. Mahesh, J. M. Ball, R. D. Oliver, D. P. McMeekin, P. K. Nayak, M. B. Johnston, H. J. Snaith. Revealing the origin of voltage loss in mixed-halide perovskite solar cells. *Energy Environ. Sci.* 13, 258-267 (2020).
- 37. R. D. J. Oliver, P. Caprioglio, F. Peña-Camargo, L. R. V. Buizza, F. Zu, A. J. Ramadan, S. G. Motti, S. Mahesh, M. M. McCarthy, J. H. Warby, Y.-H. Lin, N. Koch, S. Albrecht, L. M. Herz, M. B. Johnston, D. Neher, M. Stolterfoht, H. J. Snaith. Understanding and suppressing non-radiative losses in methylammonium-free wide-bandgap perovskite solar cells. *Energy Environ. Sci.* 15, 714-726 (2022).
- 38. T. S. Liang, M. Pravettoni, C. Deline, J. S. Stein, R. Kopecek, J. P. Singh, W. Luo, Y. Wang, A. G. Aberle, Y. S. Khoo. A review of crystalline silicon bifacial photovoltaic performance characterisation and simulation. *Energy Environ. Sci.* 12, 116-148 (2019).
- 39. R. Guerrero-Lemus, R. Vega, T. Kim, A. Kimm, L. E. Shephard. Bifacial solar photovoltaics—A technology review. *Renew. Sustain. Energy Rev.* **60**, 1533-1549 (2016).
- 40. A. Onno, N. Rodkey, A. Asgharzadeh, S. Manzoor, Z. S. J. Yu, F. Toor, Z. C. Holman. Predicted power output of silicon-based bifacial tandem photovoltaic systems. *Joule* **4**, 580-596 (2020).

- M. De Bastiani, A. J. Mirabelli, Y. Hou, F. Gota, E. Aydin, T. G. Allen, J. Troughton, A. S. Subbiah,
 F. H. Isikgor, J. Liu, L. Xu, B. Chen, E. Van Kerschaver, D. Baran, B. Fraboni, M. F. Salvador, U.
 W. Paetzold, E. H. Sargent, S. De Wolf. Efficient bifacial monolithic perovskite/silicon tandem solar cells via bandgap engineering. *Nat. Energy* 6, 167-175 (2021).
- 42. M. De Bastiani, A. S. Subbiah, M. Babics, E. Ugur, L. Xu, J. Liu, T. G. Allen, E. Aydin, S. De Wolf. Bifacial perovskite/silicon tandem solar cells. *Joule* 6, 1431-1445 (2022).
- 43. Z. Song, C. Li, L. Chen, Y. Yan. Perovskite solar cells go bifacial—Mutual benefits for efficiency and durability. *Adv. Mater.* **34**, 2106805 (2022).
- 44. K. A. Bush, A. F. Palmstrom, Z. S. J. Yu, M. Boccard, R. Cheacharoen, J. P. Mailoa, D. P. McMeekin, R. L. Z. Hoye, C. D. Bailie, T. Leijtens, I. M. Peters, M. C. Minichetti, N. Rolston, R. Prasanna, S. Sofia, D. Harwood, W. Ma, F. Moghadam, H. J. Snaith, T. Buonassisi, Z. C. Holman, S. F. Bent, M. D. McGehee. 23.6%-efficient monolithic perovskite/silicon tandem solar cells with improved stability. *Nat. Energy* 2, 17009 (2017).
- 45. B. Chen, Z. Yu, K. Liu, X. Zheng, Y. Liu, J. Shi, D. Spronk, P. N. Rudd, Z. Holman, J. Huang. Grain engineering for perovskite/silicon monolithic tandem solar cells with efficiency of 25.4%.
 Joule 3, 177-190 (2019).
- 46. R. Prasanna, T. Leijtens, S. P. Dunfield, J. A. Raiford, E. J. Wolf, S. A. Swifter, J. Werner, G. E. Eperon, C. de Paula, A. F. Palmstrom, C. C. Boyd, M. F. A. M. v. Hest, S. F. Bent, G. Teeter, J. J. Berry, M. D. McGehee. Design of low bandgap tin–lead halide perovskite solar cells to achieve thermal, atmospheric and operational stability. *Nat. Energy* 4, 939-947 (2019).
- 47. J. Werner, T. Moot, T. A. Gossett, I. E. Gould, A. F. Palmstrom, E. J. Wolf, C. C. Boyd, M. van Hest, J. M. Luther, J. J. Berry, M. D. McGehee. Improving low-bandgap tin-lead perovskite solar cells via contact engineering and gas quench processing. ACS Energy Lett. 5, 1215-1223 (2020).
- 48. B. Chen, C. Fei, S. Chen, H. Gu, X. Xiao, J. Huang. Recycling lead and transparent conductors from perovskite solar modules. *Nat. Commun.* **12**, 5859 (2021).

- 49. S. Chen, Y. Deng, X. Xiao, S. Xu, P. N. Rudd, J. Huang. Preventing lead leakage with built-in resin layers for sustainable perovskite solar cells. *Nat. Sustain.* **4**, 636-643 (2021).
- 50. S. Chen, Y. Deng, H. Gu, S. Xu, S. Wang, Z. Yu, V. Blum, J. Huang. Trapping lead in perovskite solar modules with abundant and low-cost cation-exchange resins. *Nat. Energy* 5, 1003-1011 (2020).
- 51. J. P. Singh, T. M. Walsh, A. G. Aberle. A new method to characterize bifacial solar cells. *Prog. Photovolt.: Res. Appl.* **22**, 903-909 (2014).
- 52. Z. Yu, X. Chen, S. P. Harvey, Z. Ni, B. Chen, S. Chen, C. Yao, X. Xiao, S. Xu, G. Yang. Gradient doping in Sn-Pb perovskites by barium ions for efficient single-junction and tandem solar cells.

 *Adv. Mater. 34, 2110351 (2022).
- 53. T. J. Jacobsson, A. Hultqvist, A. García-Fernández, A. Anand, A. Al-Ashouri, A. Hagfeldt, A. Crovetto, A. Abate, A. G. Ricciardulli, A. Vijayan, A. Kulkarni, A. Y. Anderson, B. P. Darwich, B. Yang, B. L. Coles, C. A. R. Perini, C. Rehermann, D. Ramirez, D. Fairen-Jimenez, D. Di Girolamo, D. Jia, E. Avila, E. J. Juarez-Perez, F. Baumann, F. Mathies, G. S. A. González, G. Boschloo, G. Nasti, G. Paramasivam, G. Martínez-Denegri, H. Näsström, H. Michaels, H. Köbler, H. Wu, I. Benesperi, M. I. Dar, I. Bayrak Pehlivan, I. E. Gould, J. N. Vagott, J. Dagar, J. Kettle, J. Yang, J. Li, J. A. Smith, J. Pascual, J. J. Jerónimo-Rendón, J. F. Montoya, J.-P. Correa-Baena, J. Qiu, J. Wang, K. Sveinbjörnsson, K. Hirselandt, K. Dev, K. Frohna, L. Mathies, L. A. Castriotta, M. H. Aldamasy, M. Vasquez-Montoya, M. A. Ruiz-Preciado, M. A. Flatken, M. V. Khenkin, M. Grischek, M. Kedia, M. Saliba, M. Anaya, M. Veldhoen, N. Arora, O. Shargaieva, O. Maus, O. S. Game, O. Yudilevich, P. Fassl, Q. Zhou, R. Betancur, R. Munir, R. Patidar, S. D. Stranks, S. Alam, S. Kar, T. Unold, T. Abzieher, T. Edvinsson, T. W. David, U. W. Paetzold, W. Zia, W. Fu, W. Zuo, V. R. F. Schröder, W. Tress, X. Zhang, Y.-H. Chiang, Z. Iqbal, Z. Xie, E. Unger. An open-access database and analysis tool for perovskite solar cells based on the FAIR data principles. Nat. Energy 7, 107-115 (2022).

- O. Dupré, B. Niesen, S. De Wolf, C. Ballif. Field performance versus standard test condition efficiency of tandem solar cells and the singular case of perovskites/silicon devices. *J. Phys. Chem.* Lett. 9, 446-458 (2018).
- N. L. Chang, J. Zheng, Y. Wu, H. Shen, F. Qi, K. Catchpole, A. Ho-Baillie, R. J. Egan. A bottom-up cost analysis of silicon-perovskite tandem photovoltaics. *Prog. Photovolt.: Res. Appl* **29**, 401-413 (2021).
- 56. Y. Fang, Q. Dong, Y. Shao, Y. Yuan, J. Huang. Highly narrowband perovskite single-crystal photodetectors enabled by surface-charge recombination. *Nat. Photonics* **9**, 679-686 (2015).
- S. Manzoor, Z. J. Yu, A. Ali, W. Ali, K. A. Bush, A. F. Palmstrom, S. F. Bent, M. D. McGehee, Z.
 C. Holman. Improved light management in planar silicon and perovskite solar cells using PDMS scattering layer. *Sol. Energy Mater. Sol. Cells* 173, 59-65 (2017).
- 58. A. M. Baldridge, S. J. Hook, C. I. Grove, G. Rivera. The ASTER spectral library version 2.0.

 Remote Sens. Environ. 113, 711-715 (2009).
- 59. S. Manzoor, J. Häusele, K. A. Bush, A. F. Palmstrom, J. Carpenter, Z. J. Yu, S. F. Bent, M. D. McGehee, Z. C. Holman. Optical modeling of wide-bandgap perovskite and perovskite/silicon tandem solar cells using complex refractive indices for arbitrary-bandgap perovskite absorbers. *Opt. Express* 26, 27441-27460 (2018).

Acknowledgments:

Funding: This material is based upon work supported by the U.S. Department of Energy's Office of Energy Efficiency and Renewable Energy (EERE) under Solar Energy Technologies Office (SETO) Agreement DE-EE0008749. The views expressed herein do not necessarily represent the views of the U.S. Department of Energy or the United States Government. We thank the financial support from the National Science Foundation under Award 2050357 for the study of light trapping structure.

Author contributions: B.C. and Z.Y. contributed equally to this work. J.H. and B.C. conceived the idea. B.C. and Z.Y. fabricated the NBG perovskite cells. B.C. fabricated bifacial all-perovskite tandem solar cells. S.C. prepared the neutral PEDOT HTLs and carried out the GIXRD measurements. J.W. carried out UPS measurement. A.O., Z.Y., and Z.C.H. carried out the annual-yield simulations of bifacial all-perovskite tandem solar modules and haze measurement. B.C. and J.H. wrote the paper, all the authors reviewed the paper.

Competing interests: A.O., Z.Y., and Z.C.H. are inventors on a patent application related to bifacial tandem photovoltaic cells and modules with application number of PCT/US2020/066470. The other authors declare that they have no competing interests.

Data and materials availability: All data are available in the main text or the supplementary materials.



Supplementary Materials for

Bifacial All-Perovskite Tandem Solar Cells

Bo Chen, Zhenhua Yu, Arthur Onno, Zhengshan Yu, Shangshang Chen, Jiantao Wang, Zachary C. Holman, Jinsong Huang*

*Corresponding author. Email: jhuang@unc.edu

This PDF file includes:

Figs. S1 to S21 Tables S1

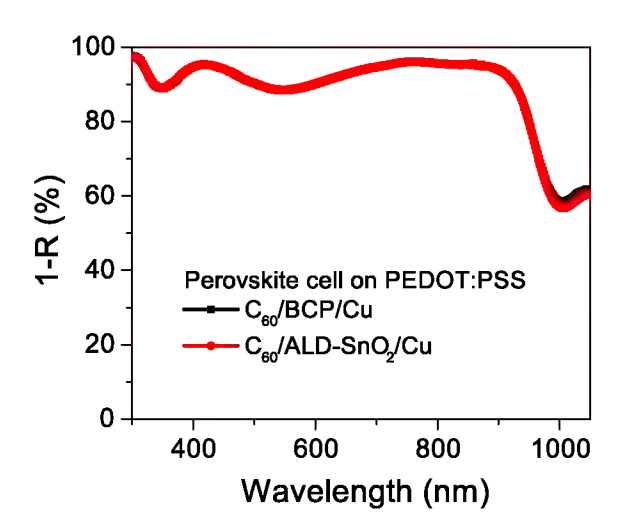


Fig. S1. Impact of ALD process on total absorptance. Total absorptance (1-R), where R is the reflectance, of Pb-Sn perovskite solar cells fabricated on acidic PEDOT:PSS with electron transport layers and cathodes consisting of C_{60} /BCP/Cu and C_{60} /ALD-SnO₂/Cu.

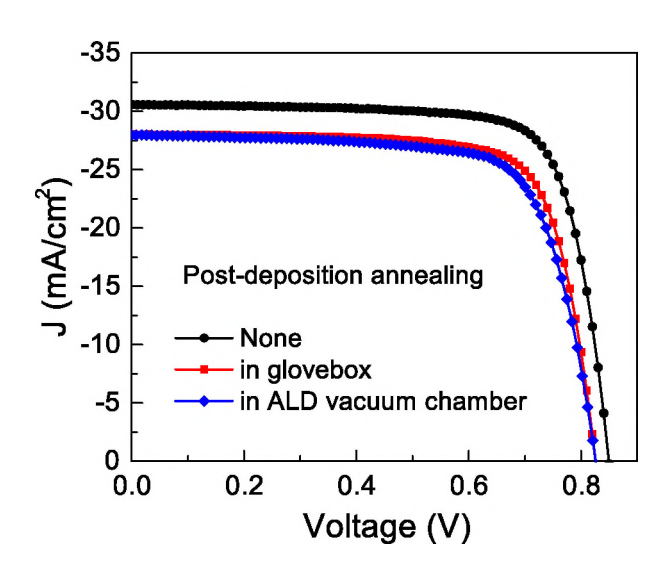


Fig. S2. Impact of post-deposition annealing on photovoltaic performance. J–V curves of Pb-Sn NBG cells fabricated on acidic PEDOT:PSS without and with post-deposition annealing. Post-deposition annealing of ITO/PEDOT:PSS/Pb-Sn samples was carried out inside N₂-filled gloveboxes at 85 °C for 150 min, followed with thermal evaporation of C₆₀/BCP/Cu. Post-deposition annealing of ITO/PEDOT:PSS/Pb-Sn perovskite/C₆₀ samples was carried out inside the ALD vacuum chamber at 85 °C for 150 min without any Sn or water precursor pulse, followed with thermal evaporation of BCP/Cu. Control sample was ITO/PEDOT:PSS/Pb-Sn perovskite/C₆₀/BCP/Cu without post-deposition of Pb-Sn perovskite film.

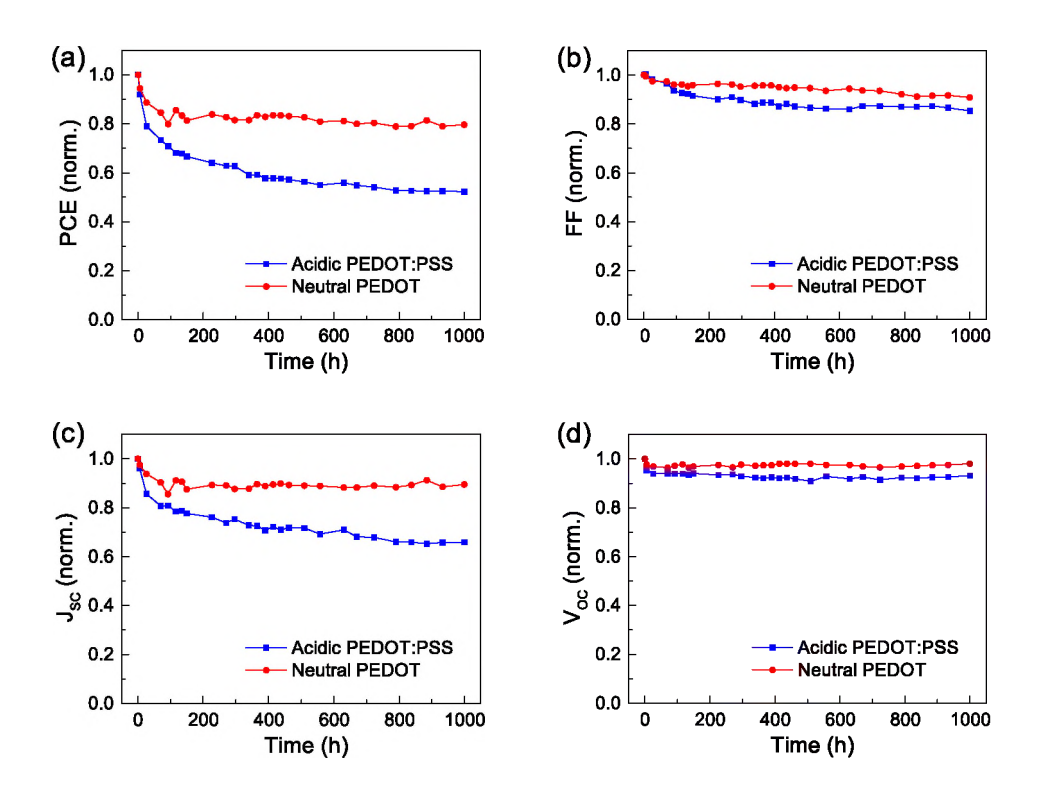


Fig. S3. Thermal stability of semi-transparent Pb-Sn cells. Evolution of photovoltaic parameters of semi-transparent Pb-Sn cells fabricated on acidic PEDOT:PSS and on neutral PEDOT during thermal stability test at 85 °C in gloveboxes for 1000 hours.

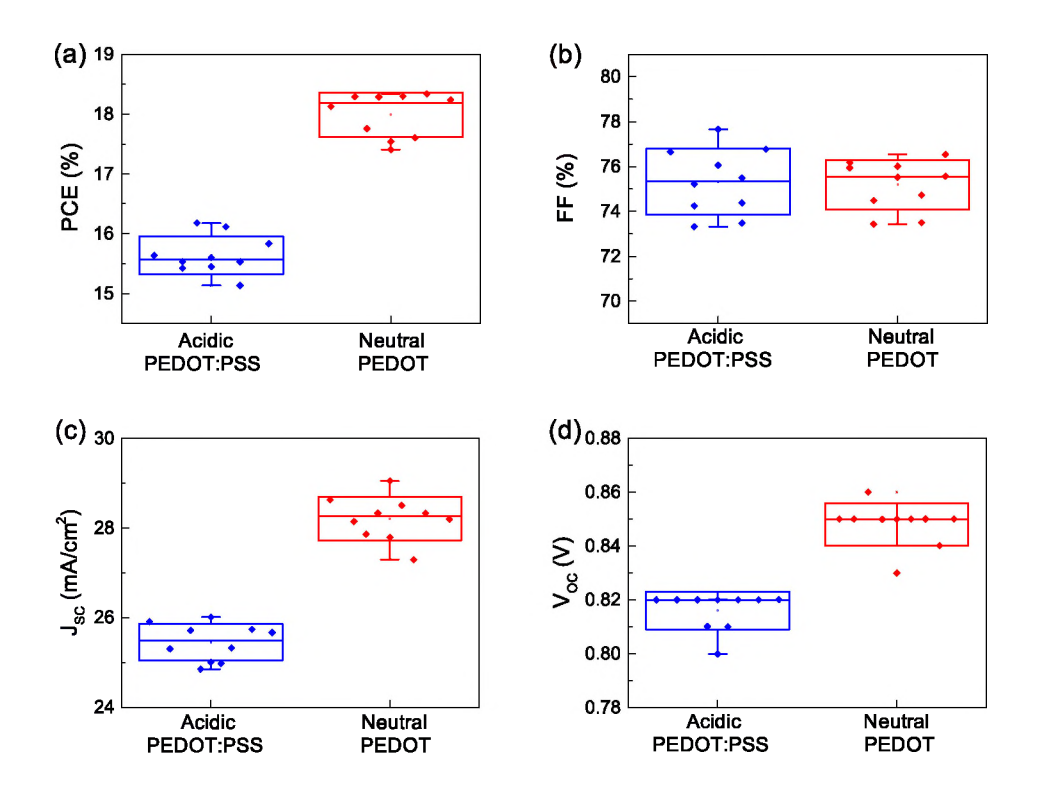


Fig. S4. Photovoltaic performance of semitransparent Pb-Sn cells on different HTLs. Photovoltaic parameter distribution of 10 semitransparent cells fabricated on acidic PEDOT:PSS and neutral PEDOT, respectively. The box indicates the standard deviation and the line inside box represents the mean value.

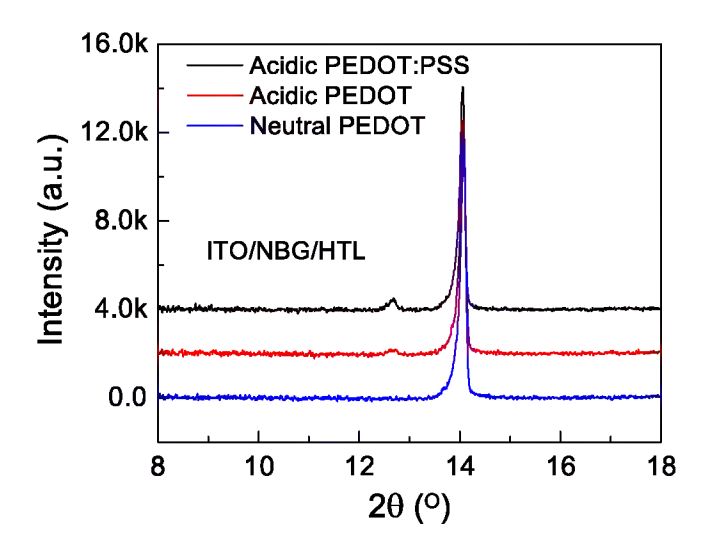


Fig. S5. Impact of HTLs on thermal stability of NBG films. XRD patterns of perovskite films with different HTLs on the top surface—with the HTLs transferred using PDMS stamps—after post-deposition annealing at 130 °C for 45 min.

To exclude the possible impact of grain size, we made Pb-Sn perovskite films all on ITO/glass substrates, where different HTLs were transferred by PDMS stamp onto the top surface of these films. Again, the PbI₂ characteristic peak at 12.7° only appeared for the perovskite films with acidic PEDOT:PSS and acidic PEDOT on top surface after post-deposition annealing, but not for the perovskite film with neutral PEDOT (Fig. S5).

To transfer the HTL, a piece of PDMS was attached to a glass substrate and treated with oxygen plasma for 30 s, the HTL solution was then spin-coated onto the PDMS substrate at 3000 rpm for 1 min and annealed at 100 °C for 5 min. The dry HTL on the PDMS substrate was subsequently transferred onto the top surface of the perovskite film, with the HTL side facing down.

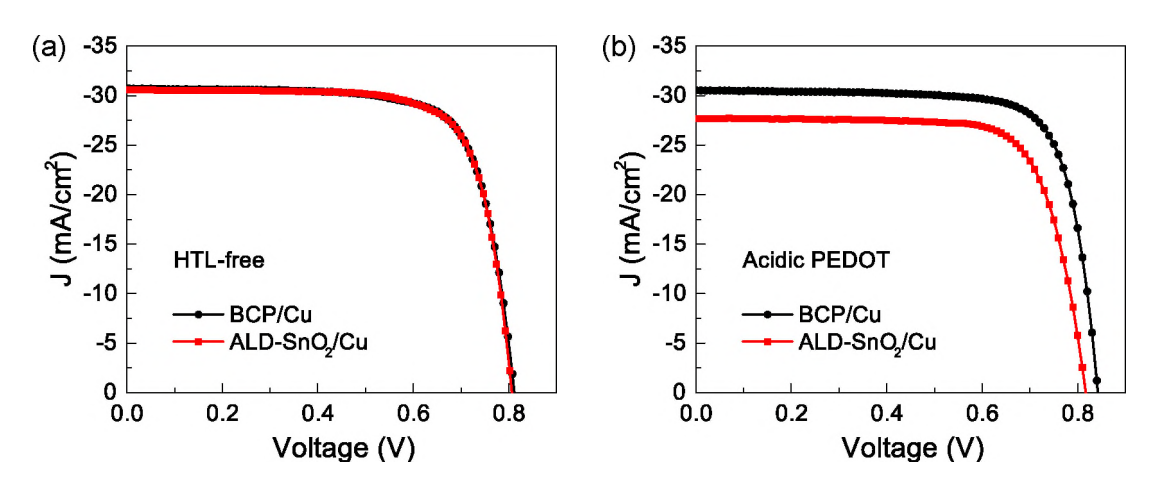


Fig. S6. Impact of HTLs on photovoltaic performance of Pb-Sn perovskite cells. J–V curves of 1.21 eV $Cs_{0.2}FA_{0.8}Pb_{0.5}Sn_{0.5}I_3$ perovskite solar cells fabricated on (a) bare ITO/glass without HTL and (b) acidic PEDOT as HTL with C_{60} /BCP/Cu and C_{60} /ALD-SnO₂/Cu electron transport layers and cathodes

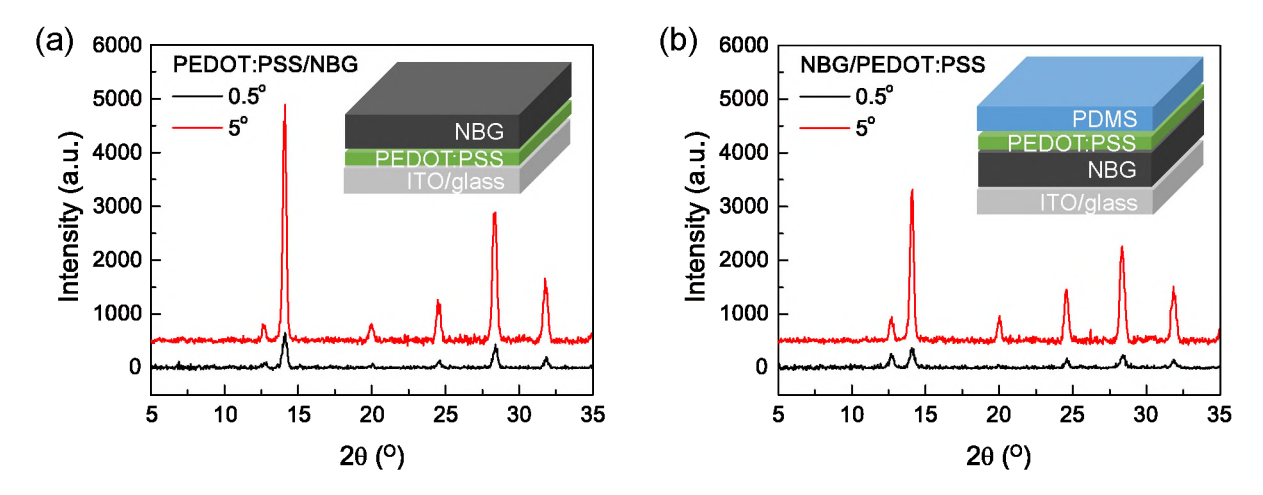


Fig. S7. GIXRD patterns of annealed Pb-Sn perovskite films with PEDOT:PSS. GIXRD patterns of Pb-Sn perovskite films with acidic PEDOT:PSS (a) at the bottom surface and (b) at the top surface (obtained by transferring a dry PEDOT:PSS film using a PDMS stamp) after annealing at 130 °C for 45 min.

Even though there was no detectable PbI₂ XRD peak formed after post-deposition annealing at 85 °C for 150 min, considering the as-fabricated sample required thermal annealing at 130 °C for 7 min, we carried out post-deposition annealing at 130 °C for longer time to amplify the possible reaction.

Grazing incidence X-ray diffraction (GIXRD) was used to determine where the formation of PbI₂ occurred. With incident angles of 0.5° and 5°, the diffraction signals are collected from the top 30 nm from the surface and from the whole 1200 nm thick film, respectively. GIXRD data in Fig. S7a shows that comparatively less PbI₂ forms in the vicinity of the top surface than in the whole film after post-deposition annealing at 130 °C for 45 min for a NBG film with acidic PEDOT:PSS at bottom surface—with a PbI₂ characteristic peak at 12.7° that is smaller with an incident angle of 0.5° than with an incident angle of 5°. On the other hand, when the PEDOT:PSS

layer is added on top surface of the perovskite film—by transferring a dry PEDOT:PSS film using a PDMS stamp—more PbI_2 forms in the vicinity of the top surface than in the whole film after post-deposition annealing at 130 °C for 45 min (Fig. S7b)— the PbI_2 characteristic peak at 12.7° is now much larger with an incident angle of 0.5°.

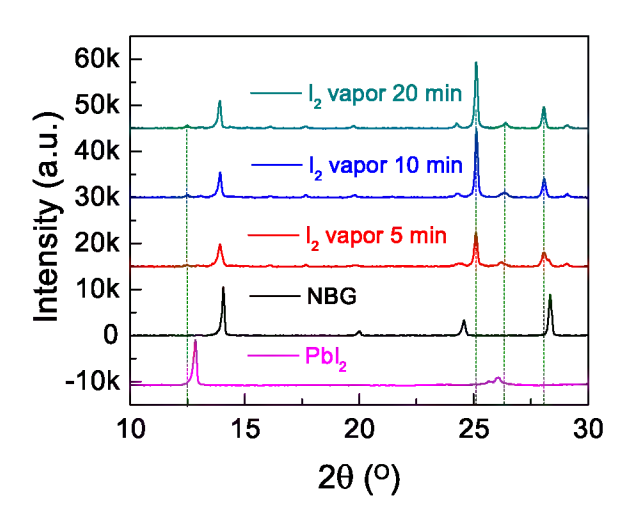


Fig. S8. Impact of I_2 vapor on Pb-Sn perovskite. XRD patterns of $Cs_{0.2}FA_{0.8}Pb_{0.5}Sn_{0.5}I_3$ NBG perovskite films after I_2 vapor treatment for different time lengths, compared with XRD patterns of the NBG perovskite film before vapor treatment and of Pb I_2 . Newly formed XRD peaks, obtained after I_2 vapor treatment, are highlighted with dashed lines.

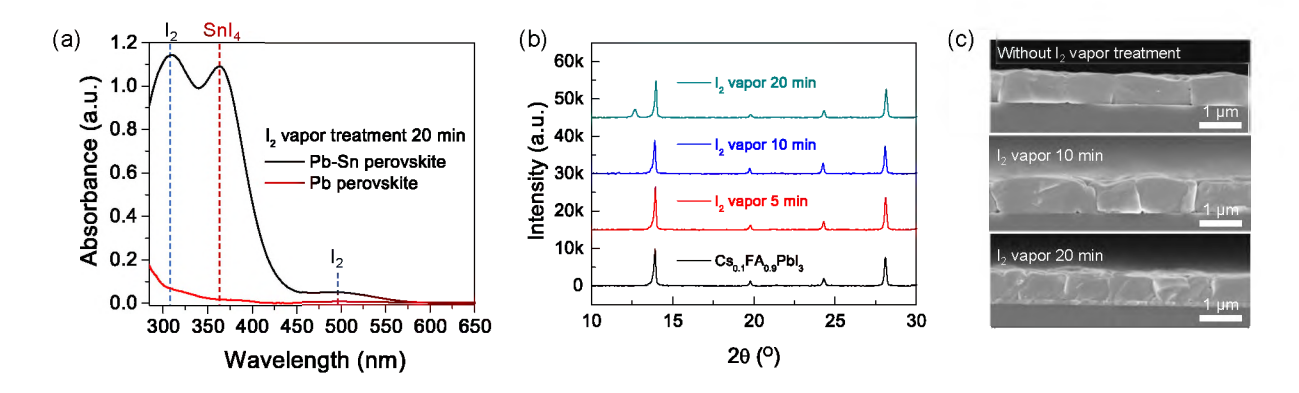


Fig. S9. Comparison of the impact of I_2 vapor on Pb-only perovskite and Pb-Sn perovskite. (a) Absorptance spectra of the reaction products of $Cs_{0.2}FA_{0.8}Pb_{0.5}Sn_{0.5}I_3$ and $Cs_{0.1}FA_{0.9}PbI_3$ perovskite films after I_2 vapor treatment (sealed with I_2 powder in vials) for 20 min. After I_2 vapor treatment, the samples were taken out from the vials and annealed at 50°C for 3 min in the glovebox in order to sublimate the adsorbed I_2 , the reaction products were then extracted for absorptance measurement using toluene. (b) XRD patterns and (c) SEM images of $Cs_{0.1}FA_{0.9}PbI_3$ perovskite films after I_2 vapor treatment.

We performed the I₂ vapor treatment on Pb-only perovskite films. The absorptance spectra in Fig. S9a show that Cs_{0.1}FA_{0.9}PbI₃ films were more resistant to I₂ vapor compared to mixed Pb-Sn perovskites. No notable amount of I₂ formed in the case of the Cs_{0.1}FA_{0.9}PbI₃ perovskite film. After 10 min of I₂ vapor treatment, XRD patterns show no change for the Cs_{0.1}FA_{0.9}PbI₃ film (Fig. S9b). After 20 min of I₂ vapor treatment, PbI₂ was the only new chemical species formed, with no other new peak. SEM images show no obvious change of the film morphology (Fig. S9c).

The Cs_{0.1}FA_{0.9}PbI₃ perovskite films were prepared at room temperature by blade coating at 20 mm/s with 250 µm of coating gap under the blowing nitrogen knife, with a precursor solution consisting of 1.0 M FAPbI₃ and 0.11 M CsPbI₃ in a 2-ME/DMSO solvent mixture. Formamidinium hypophosphite, formamidinium chloride and phenylethyl ammonium chloride were added into the

precursor solution as additives at molar percentages of $\sim 1.0\%$, $\sim 1.5\%$ and $\sim 0.15\%$ of the Pb²⁺ ions, respectively. The blade-coated films were annealed at 150 °C in air for 3 min.

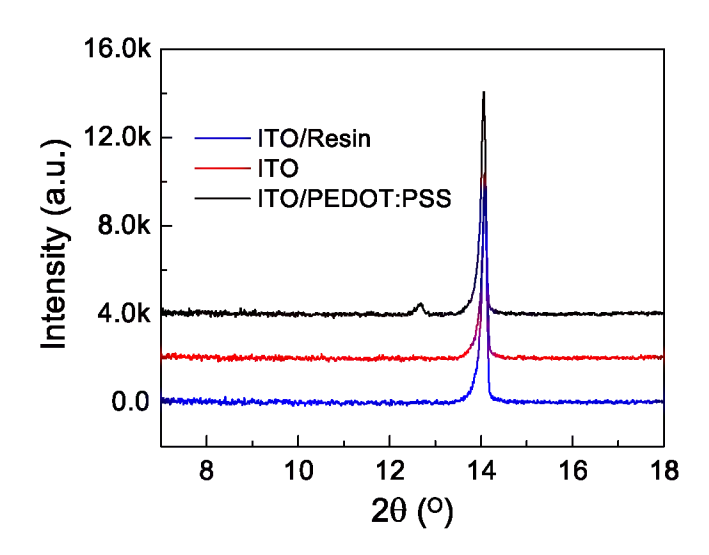


Fig. S10. Impact of resin-particle layer on thermal stability. XRD patterns of annealed perovskite films deposited on ITO/resin-particle layer, bare ITO/glass substrate, and ITO/acidic PEDOT:PSS substrate. Post-deposition annealing was carried out at 130 °C for 45 min in N_2 -filled gloveboxes.

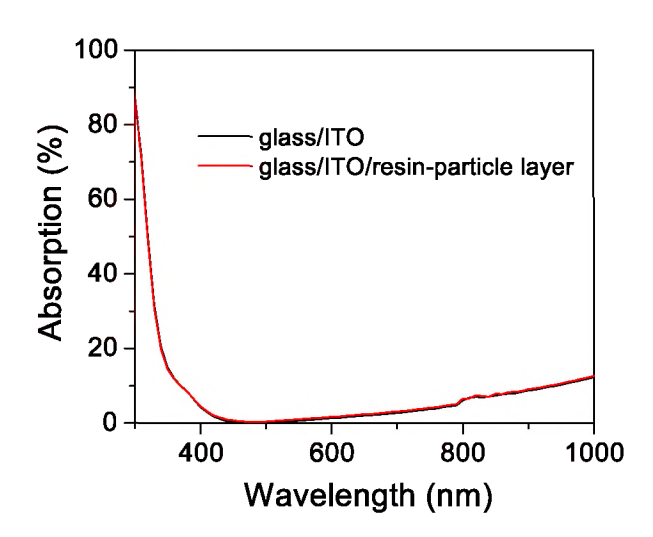


Fig. S11. Impact of resin-particle layer on absorptance. Absorptance spectra of glass (670 µm)/ITO (200 nm) substrate without and with a resin-particle layer.

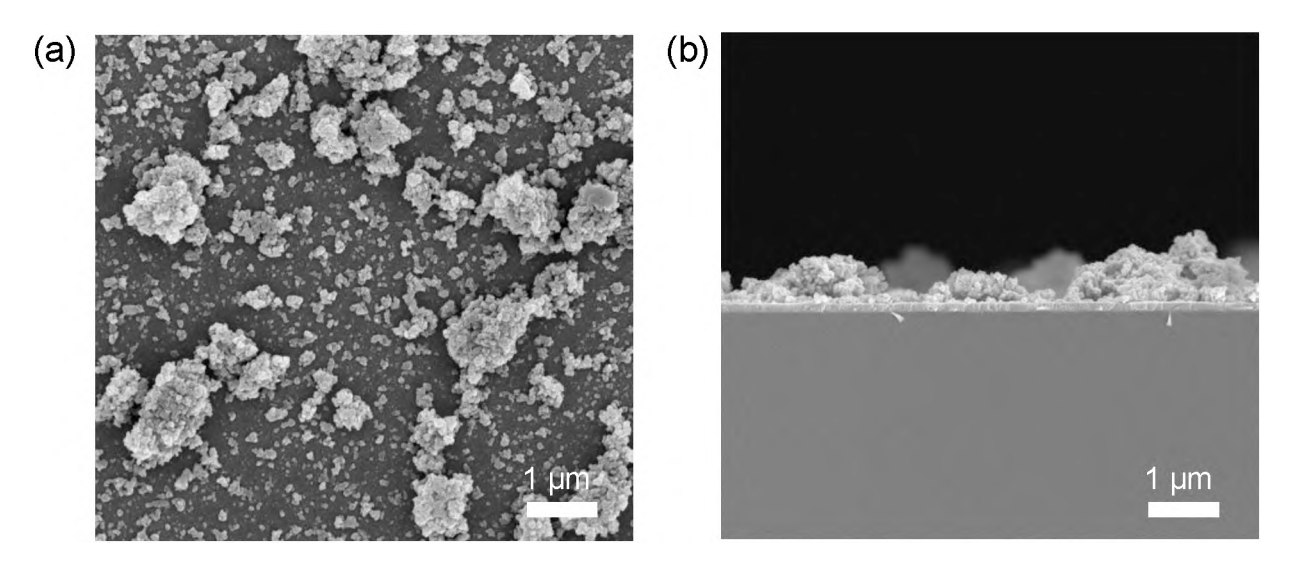


Fig. S12. Morphology of resin-particle layer. (a) Top-view surface SEM image and (b) cross-sectional SEM image of resin-particle layer on ITO/glass substrate.

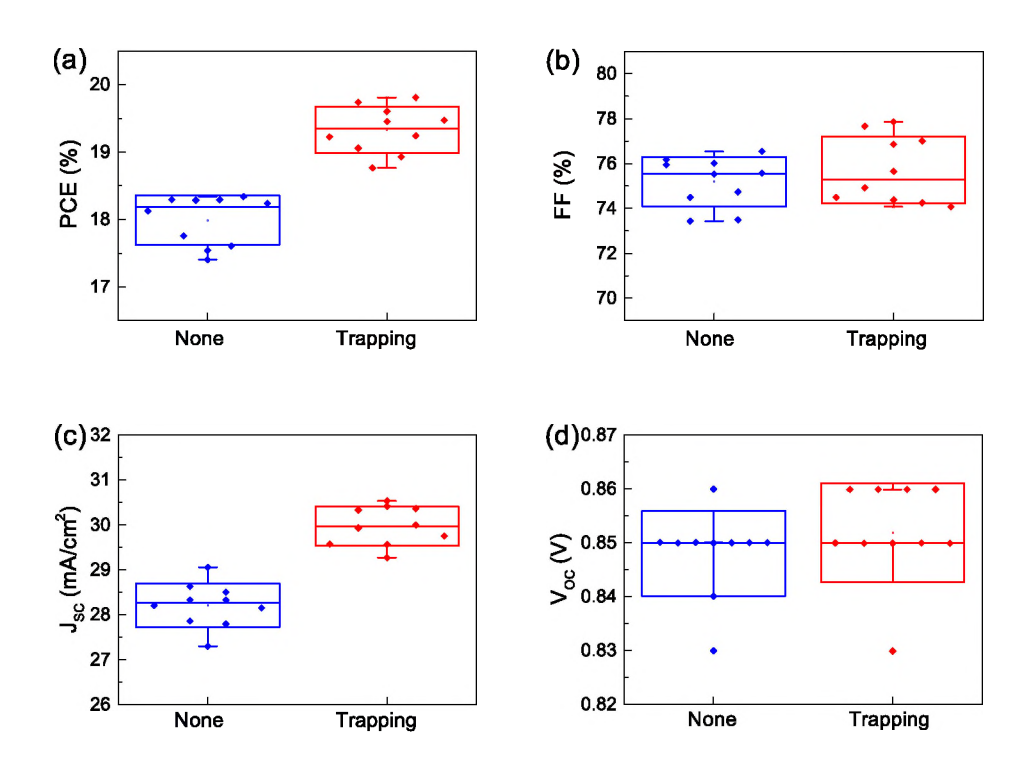


Fig. S13. Impact of light-trapping resin-particle layer on photovoltaic performance.

Photovoltaic parameter distribution of 10 semitransparent Pb-Sn single junction cells on neutral PEDOT with and without light-trapping resin-particle layer under front illumination. The box indicates the standard deviation and the line inside box represents the mean value.

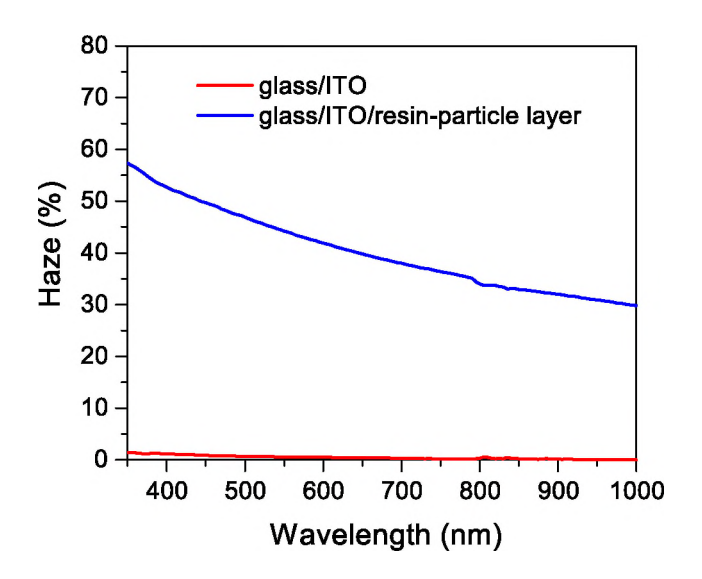


Fig. S14. Haze effect of resin-particle layer. Measured haze of glass/ITO substrate without and with resin-particle layer.

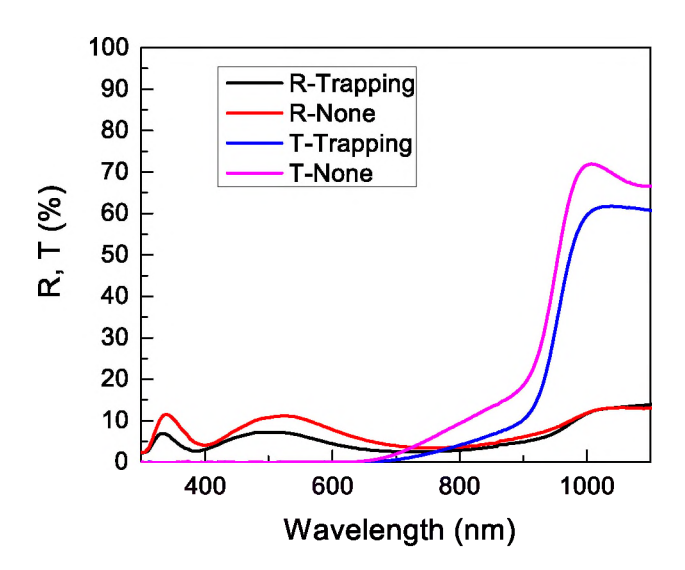


Fig. S15. Impact of resin-particle layer on reflectance and transmittance. Reflectance (R) and transmittance (T) of semitransparent Pb-Sn single junction cells on neutral PEDOT with and without light-trapping resin-particle layer under front illumination.

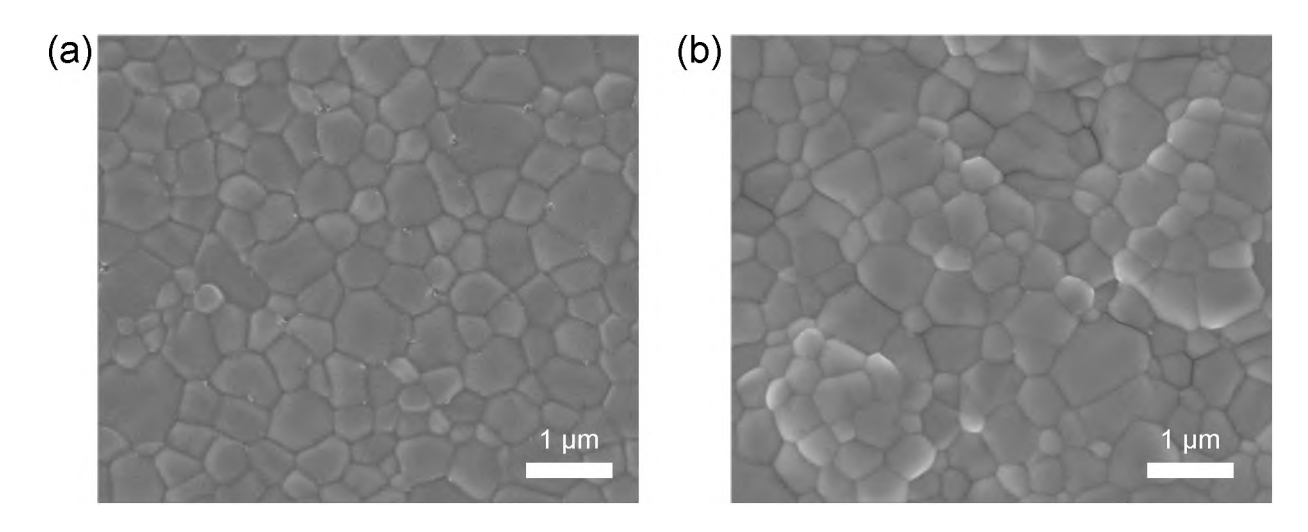


Fig. S16. Impact of light-trapping resin-particle layer on perovskite film morphology. SEM image of Pb-Sn perovskite films deposited on neutral PEDOT (a) without and (b) with light-trapping resin-particle layer.

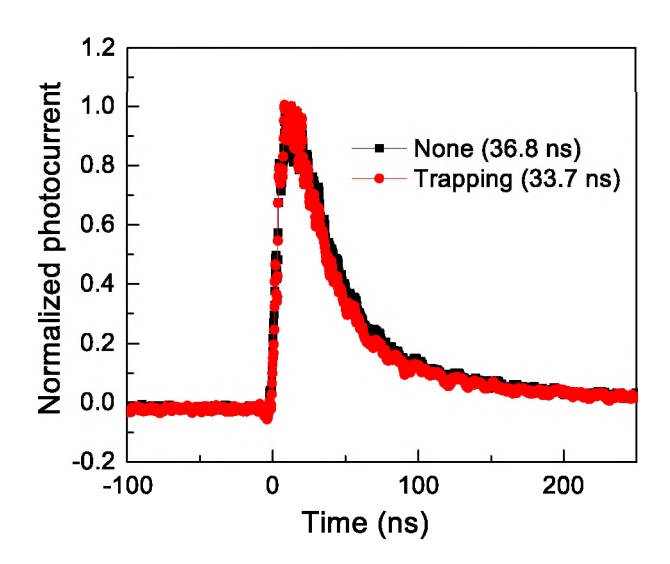


Fig. S17. Impact of light-trapping resin-particle layer on transient photocurrent result. Normalized transient photocurrent (TPC) of semitransparent Pb-Sn perovskite cells without and with light-trapping layer. The device size for TPC measurement was reduced by scribing with a knife to reduce the capacitor to <100 pF for a RC constant of <5 ns. Laser pulse during TPC measurement was illuminated from the glass/ITO/HTL side.

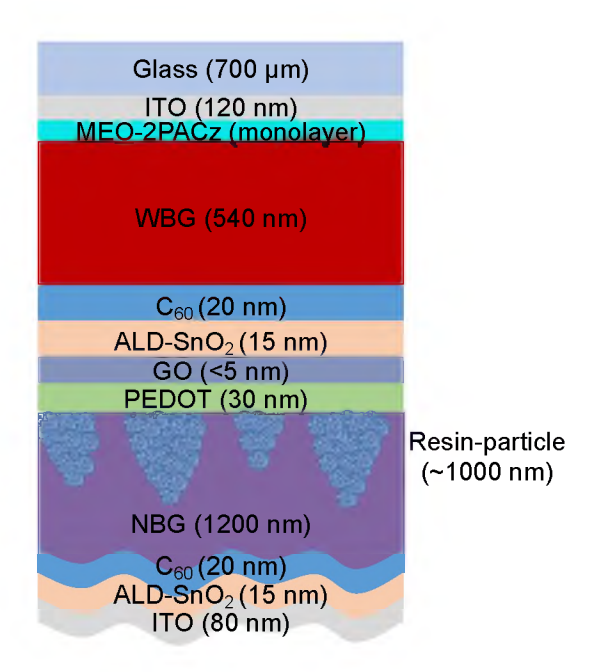


Fig. S18. Structure of bifacial all-perovskite tandem solar cells. Schematic of the stack of fabricated bifacial all-perovskite tandem solar cells with material and thickness of each layer.

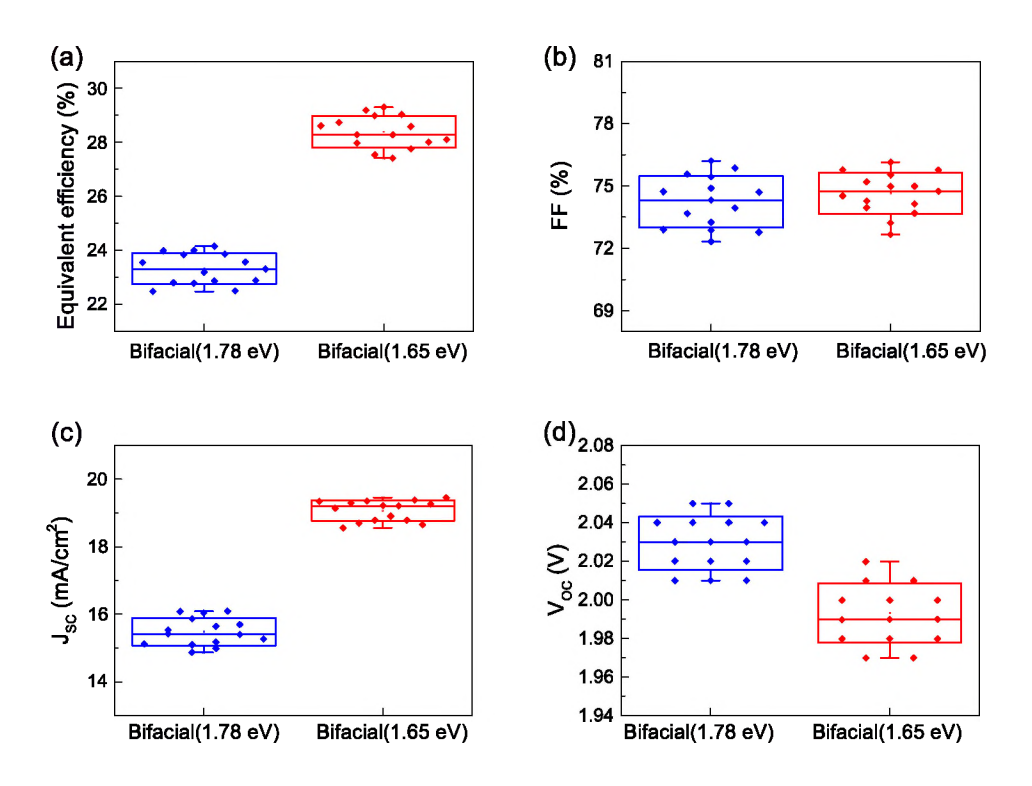


Fig. S19. Photovoltaic performance of bifacial all-perovskite tandems. Photovoltaic parameter distribution of 15 bifacial tandems fabricated in same batch with 1.78-eV and 1.65-eV WBG top cells under illumination with 30% of albedo light, where the box indicates the standard deviation and the line inside box represents the mean value.

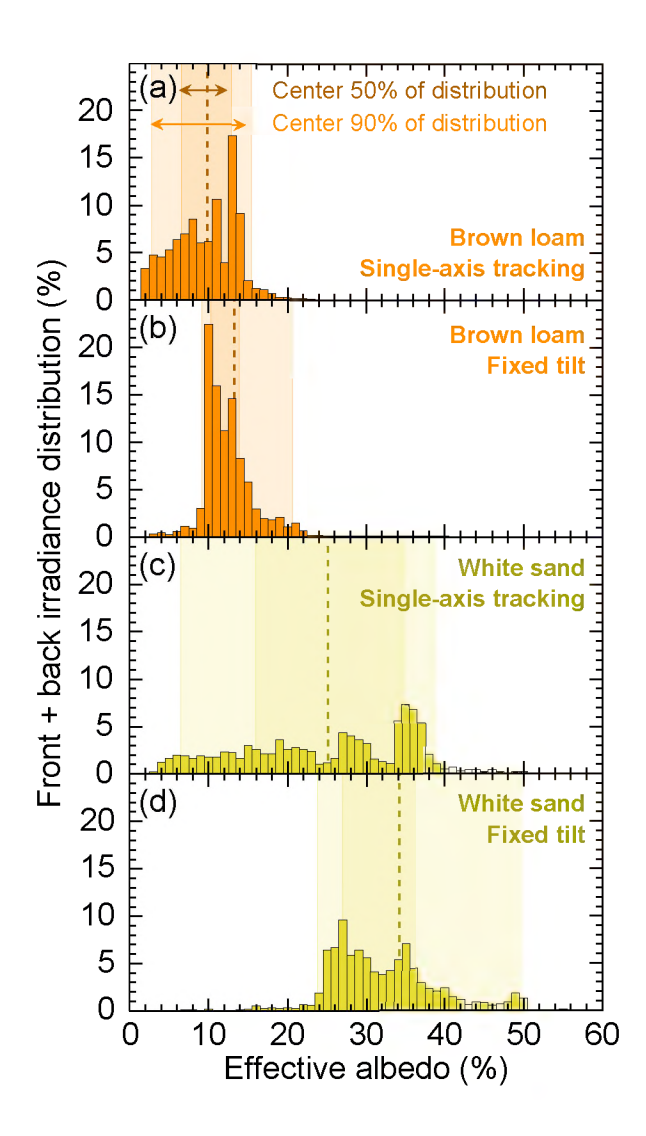


Fig. S20. Effective albedo at different conditions. Distributions in power of the effective albedo in a photovoltaic power plant installed in Phoenix on (a,b) brown loam and (c,d) white sand with single-axis-tracking (a,c) and fixed-tilt (b,d) systems.

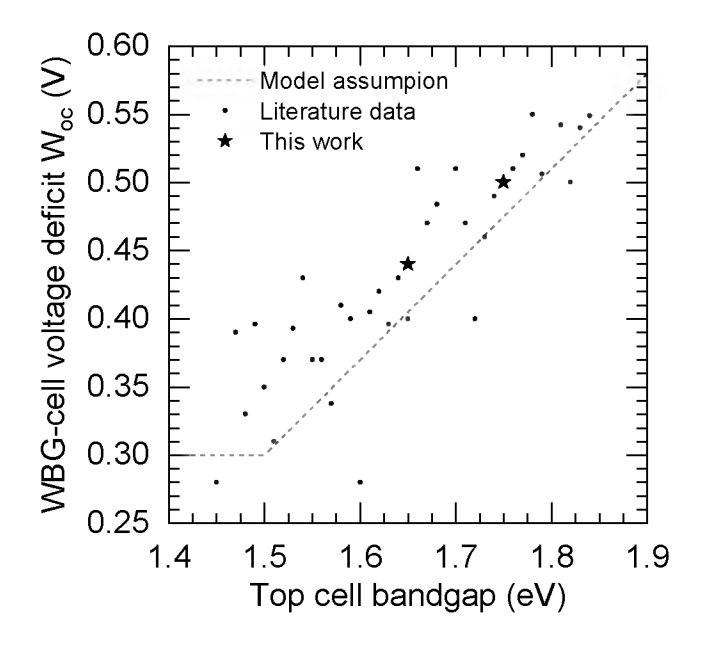


Fig. S21. Reported experimental W_{OC} values and model assumption. Voltage deficit W_{OC} values (dots) of the best WBG perovskite solar cells reported in the perovskite database from reference 53. The stars correspond to the W_{OC} achieved with semi-transparent WBG cells in this study. The dashed line shows the relation between the W_{OC} and the bandgap of the WBG cell assumed in our simulations of mono-facial and bifacial tandem devices.

Table S1. Reported experimental W_{OC} values of WBG cells. Summary of bandgap, W_{OC} , and V_{OC} for the WBG perovskite solar cells from reference 53 shown in Fig. 4c-f and Fig. S21.

Bandgap (eV)	Woc (V)	Voc (V)
1.45	0.28	1.17
1.45	0.28	1.17
1.47	0.39	1.08
1.48	0.33	1.15
1.49	0.396	1.094
1.5	0.35	1.15
1.51	0.31	1.2
1.52	0.37	1.15
1.53	0.393	1.137
1.54	0.43	1.11
1.55	0.37	1.18
1.56	0.37	1.19
1.57	0.338	1.232
1.58	0.41	1.17
1.59	0.4	1.19
1.6	0.28	1.32
1.61	0.405	1.205
1.62	0.42	1.2
1.63	0.396	1.234
1.64	0.43	1.21
1.65	0.4	1.25
1.66	0.51	1.15
1.67	0.47	1.2
1.68	0.484	1.196
1.7	0.51	1.19
1.71	0.47	1.24
1.72	0.4	1.32
1.73	0.46	1.27
1.74	0.49	1.25
1.75	0.502	1.248
1.76	0.51	1.25
1.77	0.52	1.25
1.78	0.55	1.23
1.79	0.506	1.284
1.81	0.542	1.268
1.82	0.5	1.32
1.83	0.54	1.29
1.84	0.549	1.291